TURUN YLIOPISTON JULKAISUJA
ANNALES UNIVERSITATIS TURKUENSIS

SARJA - SER. A I OSA-TOM.
ASTRONOMICA-CHEMICA-PHYSICA-MATHEMATICA

SUPERCONDUCTING PROPERTIES AND THEIR ENHANCEMENT IN *RE*$Ba_2Cu_3O_{7-\delta}$ (*RE* = Y and Gd) FILMS PREPARED BY PULSED LASER DEPOSITION

by

Kim Schlesier

TURUN YLIOPISTO
Turku 2010

From the Wihuri Physical Laboratory
Department of Physics and Astronomy
University of Turku
Turku, Finland
and
Graduate School of Materials Research
Turku, Finland

Supervised by

Professor Reino Laiho and Adjunct Professor Petriina Paturi
Wihuri Physical Laboratory
Department of Physics and Astronomy
University of Turku
Turku, Finland

Reviewed by

Dr. Nicholas Strickland
Industrial Research Ltd
PO Box 31310
Lower Hutt 5040
New Zealand

Dr. Adrian Crisan
School of Metallurgy and Materials
The University of Birmingham
Edgbaston
Birmingham
B15 2TT
United Kingdom

Opponent

Dr. Jean-Claude Grivel
Technical University of Denmark
Risø National Laboratory for Sustainable Energy
Materials Research Division
P.O. Box 49
Frederiksborgvej 399
DK-4000 Roskilde
Denmark

ISBN 978-951-29-4378-4 (PRINT)
ISBN 978-951-29-4379-1 (PDF)
ISSN 0082-7002

Acknowledgements

This work has been carried out in Wihuri Physical Laboratory at the university of Turku. I wish to thank Graduate School of Materials Research, Antti and Jenny Wihuri Foundation, Oiva Järitty Foundation and Magnus Ehnrooth Foundation for financial support.

I would like to thank my supervisor, prof. R. Laiho for giving me an opportunity to work as a doctoral student in his group and for arranging all the financing. Without his wisdom and experience, I could not have even started my post-graduate studies. I also would like to thank adjunct prof. P. Paturi for her wonderful guidance, great ideas, vital feedback and supervision of high standard. Without her, I would not ever have completed my PhD. I express my gratitude to my opponent, Dr. J.-C. Grivel: I could never have imagined to have such a brilliant scientist as my opponent. I'm grateful to Dr. N. Strickland and Dr. A. Crisan for reviewing my dissertation. I also wish to thank them for their valuable and encouraging feedback. I would like to thank Dr. H. Huhtinen for his guidance in science and life in general: from him I have got many gold grains into my 'lunch box of life'. He has always been there to help and encourage me when needed. I would like thank Dr. Yu.-P. Stepanov for making all the GdBCO targets, and Dr. S. Granroth for making the XPS measurements. I am very thankful to the rest of the staff in Wihuri Physical Laboratory, especially to MSc I. Ojala and MSc M. Irjala for their help, valuable conversations and lunch company. I am sincerely grateful to E. Lilja, for without his hard work and long working days my measurements would have been stalled many times. I wish to thank prof. A. V. Narlikar who not only advised me to enjoy the research – the advice which has guided me ever since – but has done a lot to make that a reality.

I express my gratitude to all of my friends, who have brought joy into my life and who have listened to my worries during these years.

I thank all my family and relatives for their love and support. I especially wish to thank my mother for all the sacrifices she has made for me and my brother – our happiness has always come first in her life.

Finally, I thank the Heavenly Father for this miracle to come true. Without feeling His love I would not be 'still standing'.

Turku, August 2010

Kim Schlesier

Abstract

The undoped and 4 wt% $BaZrO_3$ (BZO)-doped $ReBa_2Cu_3O_{7-\delta}$ (Re = Y and Gd) (ReBCO) high temperature superconductor (HTS) thin films were made by pulse laser deposition (PLD) method on $SrTiO_3$ (STO) (100) substrates from targets of nanosized grains. Their structure and superconductivity properties were studied with x-ray diffraction (XRD) and magnetisation measurements. The pinning potential U_0 was determined by resistivity measurements in temperature activated flux-flow (TAFF) regime. The irreversibility field B_{irr} was determined with resistivity studies, as well as the magnetic field angle dependence of resistivity was investigated at high temperatures. The results show that the optimum deposition temperature was lower, 700°C for GdBCO comparing with 745°C for YBCO. The best obtained critical current densities, J_{c}'s, were higher for undoped GdBCO than for undoped YBCO at 10 K, as well as at 77 K. The BZO doping enhanced the J_{c} at low temperatures and at high fields, where the enhancement was higher for BZO doped GdBCO, either at low temperatures or high temperatures. The U_0 and B_{irr} were improved for both the materials by BZO doping in $B \parallel c$ but decreased in $B \perp c$-direction. Also, U_0 was lower for undoped GdBCO than YBCO in $B \perp c$-direction. The reason for this was explained by distortion of the CuO_2-layers, lowering the intrinsic pinning. The undoped GdBCO was found to be more isotropic than YBCO, similarly the doped materials were more isotropic than undoped ones, at high temperatures.

The growth mechanism and pinning properties of YBCO/BZO multilayers were systematically studied. The results show that the pinning and structural properties depend on the YBCO and BZO layer thicknesses, hence the structure should be optimised for desired thin film properties. The multilayer structure with very thin multilayers was the only one that could match the properties of BZO doping with one mixed target. This would result in alignment of the BZO particles in quasi-layers.

The observed aging effect of GdBCO was systematically studied. The superconducting properties, T_{c} and J_{c} with magnetisation measurements, and the structural properties with XRD were determined for uncoated and Au-coated GdBCO and YBCO, being measured in one month intervals for five months. An x-ray photoelectron spectroscopy (XPS) study was also made for fresh and seven months old GdBCO thin film sample in order to study the oxygen content in the bulk near surface. The origin of the aging effect was attributed to oxygen release.

Preface

List of Abbreviations and Symbols

AFM	atomic force microscopy
BE	binding energy (keV)
BZO	$BaZrO_3$
CC	coated conductor
FWHM	full-width at half-maximum, i.e. the peak width
GdBCO	$GdBa_2Cu_3O_{7-\delta}$
HTS	high temperature superconductor
PLD	pulsed laser deposition
ReBCO	$ReBa_2Cu_3O_{7-\delta}$ (Re = Y, Pr, Nd, Sm, Eu, Gd, Ho . . .)
SC	superconductor
STO	(100) oriented $SrTiO_3$
TAFF	temperature activated flux-flow
XPS	x-ray photon electrons spectroscopy
XRD	x-ray diffraction
YBCO	$YBa_2Cu_3O_{7-\delta}$
YSZ	yttrium stabilised zirconium
a, b	length and width of the rectangular film in Bean model (m)
a, b, c	lattice parameters (Å)
B	magnetic induction (T)
B^*	accommodation field, $B^* \leq B_\phi$
B_{irr}	irreversibility field
B_ϕ	matching field i.e. the field where number of vortices matches the number of pinning sites
F_{L}	Lorentz-force
F_{p}	pinning force
H	applied magnetic field (A/m)
H_{c}	critical field
H_{c1}	lower critical field of type II superconductor
H_{c2}	upper critical field of type II superconductor
I	current (A)
$I(00l)$	intensity of (00l) (l = 4, 5 or 7) reflection in XRD
I_{c}	critical current (A)
J_{c}, j_{c}	critical current density (A/cm^2)

k, m, n	number of layers, and number of shot pulses, respectively
M'	real part of ac-magnetisation (Am^2)
r_c	lattice coherence length (nm)
T_c	critical temperature
T_s	substrate deposition temperature
T_0	fitting parameter (K) in equation (11) on page 35 and in equation (12) on page 38
U	pinning potential
α	exponent in equation (4) on page 3
β	exponent in equation (13) on page 46
δ	oxygen deficiency
$\Delta\omega$	the full-width at half-maximum of a rocking-curve
ε_r	pinning energy
ε_0	vortex energy, $\varepsilon_0 = [\phi_0/(4\pi\lambda)]^2$
Θ	rotation angle in degrees
θ	Bragg angle in degrees
λ	London penetration depth
ξ	coherence length
ρ	resistivity ($\mu\Omega cm^2$)
ρ_N	normal state resistivity ($\mu\Omega cm^2$)
ϕ	rotation angle
ϕ_0	magnetic flux quantum, $\approx 2.07 \cdot 10^{-15}$ Wb
χ	susceptibility
ψ	tilt angle
ω	rocking angle

Articles included in this thesis

[**P1**] K. Schlesier, H. Huhtinen, P. Paturi, Yu. P. Stepanov and R. Laiho, *Structural and superconducting properties of undoped and BZO-doped GdBCO thin films*, IEEE Transactions on Applied Superconductivity, **19(3)** (2009) 3407

[**P2**] P. Paturi, K. Schlesier and H. Huhtinen, *Effect of target density on YBCO thin films deposited from nanograined targets*, Physica C, **469** (2009) 839

[**P3**] H. Huhtinen, K. Schlesier and P. Paturi, *Growth and c-axis flux pinning of nanostructured YBCO/BZO multilayers*, Superconductor Science and Technology, **22** (2009) 075019

[**P4**] K. Schlesier, H. Huhtinen, S. Granroth, and P. Paturi, *An aging effect and its origin in GdBCO thin films*, Journal of Physics: Conference series, **234** (2010) 012036

[**P5**] K. Schlesier, H. Huhtinen, and P. Paturi, *Reduced intrinsic and strengthened columnar pinning of undoped and 4 wt% $BaZrO_3$-doped $GdBa_2Cu_3O_{7-\delta}$ thin films: a comparative resistivity study near T_c*, Superconductor Science and Technology, **23** (2010) 055010

Articles relevant to this work but not included in this thesis

[**P6**] J. Raittila, T. Salminen, T. Suominen, K. Schlesier and P. Paturi, *Nanocrystalline $Sr_2FeMoFeO_6$ prepared by citrate-gel method*, Journal of Physics and Chemistry of Solids, **67** (2006) 1712

[**P7**] T. Suominen, J. Raittila, T. Salminen, K. Schlesier, J. Lindén and, P. Paturi, *Magnetic properties of fine SFMO particles: Superparamagnetism*, Journal of Magnetism and Magnetic Materials, **309** (2007) 278

[**P8**] K. Schlesier, V.P.S. Awana, Jyoti Shah, H. Kishan, I. Felner, A.V. Narlikar, and R. Laiho, *Magnetizaion and ferromagnetic resonance (FMR) studies on $RuSr_2$-$(Eu_{1.5}Ce_{0.5})Cu_2O_{10}$ magneto-superconductor*, Physica C, **460-462** (2007) 513

[**P9**] A. Gupta, H. Huhtinen, C. Shekhar, K. Schlesier, P. Srivastava, A. Srivastava, O. N. Srivastava, R. Laiho, and A. V. Narlikar, *Occurrence of superconductivity and magnetism in nominally undoped LaOFeAs*, Journal of Superconductivity and Novel Magnetism, (In print)

Contents

1 Introduction

1.1 Superconductivity

1.1.1 Basic properties

Superconductivity was first found in Leiden in 1911 by Heike Kamerlingh Onnes, when he was measuring the resistivity of mercury. He discovered that at 4.19 K, just below boiling point of liquid He, which is 4.2 K, the resistivity of Hg dropped to zero [1]. This temperature is called the critical temperature, T_c. Zero resistivity is the first of two criterion that a superconductor must fulfil.

The second criterion is the perfect diamagnetism which means that the susceptibility, χ, of the superconducting material has to be exactly -1. In other words, a magnetic field cannot penetrate a superconductor. This phenomenon is called the Meissner–Ochsenfeld effect, after its discoverers [2].

The argument of a magnetic field not penetrating the whole superconductor (SC) is not exactly valid. Actually, the magnetic field can penetrate a small length on the surface of the SC. This is called the London penetration depth, λ [3]. It can be easily derived from Maxwell's equations just by presuming zero resistivity and perfect diamagnetism. Although the model is simple, it explains the Meissner–Ochsenfeld-effect.

Moreover, the perfect zero resistivity and diamagnetism apply only to a certain type SC's, and since they are the first ones discovered, they are called the type one SC's. Above the critical field, H_c they have a normal resistive phase. H_c has the temperature dependence:

$$H_\mathrm{c}(T) = H_\mathrm{c}(0)\left[1 - \left(\frac{T}{T_\mathrm{c}}\right)^2\right], \tag{1}$$

where $H_\mathrm{c}(0)$ is the critical field at absolute zero [4]. H_c is typically rather small, and hence this class of materials has no applications of interest.

For applications, type two SC's are more interesting, since they have two critical fields, $H_{\mathrm{c}1}$ and $H_{\mathrm{c}2}$ where the upper one can be huge, even hundreds of Teslas. The temperature dependence of both is similar to H_c in equation (1) [4]. The lower critical field is rather low, and in thermodynamic sense it is lower than H_c of the type one SC's. Below $H_{\mathrm{c}1}$ the Meissner-state with no magnetic field inside the SC exists. Between $H_{\mathrm{c}1}$ and $H_{\mathrm{c}2}$ is so called mixed state, where magnetic field can penetrate the superconducting media by forming vortices i.e. fluxons, which have a constant value of magnetic flux i.e. a flux quantum: $\phi_0 = h/(2e) = 2.07 \cdot 10^{-15}$ Wb.

In case of weak or no pinning, the distance between vortices is higher than λ at rather

low fields, therefore the vortices do not interact with each other. Then, the vortices are randomly distributed and the phase is called as *vortex liquid* [5].

As the magnetic field and hence the number of vortices is increased, the vortices will align hexagonally in case of no pinning, since the vortices repel each other. The phase is called as *vortex lattice* [5]. Also, if the current density J is also applied, the vortices start to move, due to the Lorentz-force $\boldsymbol{F}_{\mathrm{L}} = \boldsymbol{J} \times \boldsymbol{B}$. The movement of vortices dissipates energy which is seen as a voltage indicating an ohmic resistance, hence the zero resistive superconducting state is lost. At high magnetic fields, relatively high temperatures, and with $F_{\mathrm{L}} = 0$, the temperature fluctuation cause the lattice to melt, the order is lost, therefore the phase is called *vortex liquid*, too.

1.1.2 Flux pinning

Usually, some pinning sites are present, and these pin the vortices with pinning force F_{p}. Such pinning sites are for example point like defects. The F_{p} of a single point-like pinning site is rather small, but a vortex can adjust within a network of point-like pins to gain pinning force to overcome F_{L} with expense of elastic energy. However, they trap only a fraction of the vortex, and therefore they are considered *weak pinning* sites. At relatively low temperatures, the pinning force is much larger than F_{L}, the vortices are trapped to pinning sites, therefore the long range aligned vortices lattice is distorted, and vortices have only a short range alignment, hence the phase is called as the *vortex glass* phase. As the magnetic field or temperature is increased, the pinning force becomes smaller than the Lorentz-force which although still dominates over the temperature fluctuations, and the alignment of the vortices is lost, hence the phase is called the *pinned liquid* phase. The cross-over of these two latter phases is separated by irreversibility line H_{irr}(T) or temperature T_{irr}(H). Below this line a zero resistivity is reached with small currents and a hysteresis is present in magnetisation measurements. As the magnetic field is further increased but is still lower than H_{c2}, the vortices start to flow freely, since the temperature fluctuations dominate over F_{p}, hence this vortex phase is called the *flux-flow* regime.

The pinning sites are considered strong, if a point-like pinning site can induce plastic deformation in the vortex lattice or if the pinning site extends to the whole vortex length. Correlated pinning sites can be such as planes and rods. In low temperature region, the vortices will pin to a free, strong pinning sites until the magnetic field reaches the so called accommodation field

$$B^* = \frac{4\varepsilon_r}{\varepsilon_0} B_\phi, \tag{2}$$

where $B_\phi = n\phi_0$ is the matching field, ε_r is the pinning energy (or potential), and ε_0 is the vortex energy scale, $\varepsilon_0 = [\phi_0/(4\pi\lambda)]^2$ [5]. Above B^* the plastic and collective pinning takes place. In experimental papers, B^* is usually defined by criterion [6, 7]

$$\frac{J_\mathrm{c}(B^*)}{J_\mathrm{c}(0)} = 0.9. \tag{3}$$

Above B^* the J_c can be described with power law

$$J_\mathrm{c}(B) = A(T)B^{\alpha(T)}, \tag{4}$$

where $A(0)$ is proportional to J_c(0), which is usually a decade smaller than predicted depairing current $j_\mathrm{c}(0)$ due to the non-perfect pinning [8]. In literature, there are predictions of separate regions giving different α's. Nelson *et al.* predicted $\alpha = -0.5$ in intermediate magnetic field range by presuming that only small fraction of vortices are pinned directly, whereas the rest are pinned by shear interaction with strongly pinned vortices. This is called the *plastic pinning* [5]. In high magnetic field range, $\alpha = -1.0$ was predicted by assuming collective pinning of a vortex bundle. Van der Beek *et al.* predicted a similar $\alpha = -0.63$ for intermediate field range and the same $\alpha = -1.0$ at high field range [9]. Also, Blatter *et al.* have predicted $\alpha = -0.5$ for strong pinning [10]. In addition to the former, Klaassen *et al.* also stated that samples with high defect density have a negative tendency of $\alpha(T)$ with temperature [11].

The large $\alpha \approx -0.2$ for BZO doped YBCO has been described theoretically by Paturi *et al.* [12]. They used a model where columnar defects form a triangular lattice which creates a potential well whose height is compared with elastic energy of the lattice (the energy loss which is due to distortion of Abrikosov-lattice). Then, pinned vortices are those whose distance to a pinning site is low enough to overcome the elastic energy. In this model, the critical current is simply proportional to the pinned–unpinned-vortex-ratio. Thus, the high α is due to high B_ϕ (proportional to number of defects) and a high pinning potential of the non-randomly aligned defects.

1.1.3 Temperature activated flux-flow (TAFF)

The pinning force of pinning sites correspond to a potential U_p or barrier which vortices need to cross in order to depin. At the spin glass state, the U_p can be considered infinite, and the resistivity is zero with low enough currents as stated in the previous section. Just above the melting temperature, T_m, the temperature activated vortex movement is high enough to allow the vortices to creep over the barrier, but they are still bound to pinning sites, and hence this regime is called the temperature activated flux flow

(TAFF), or ordered vortex liquid. In addition, the pinning potential is also lowered with the Lorentz-force, $F_{\mathrm{L}} = J \times B$, by potential $U_{\mathrm{L}} = J \times B V_c r_p$, where V_c is the volume of the flux bundle, and r_p is the range of the pinning potential [13]. The resistivity depends linearly on the current but exponentially on the temperature:

$$\rho = \rho_{0f} \exp\left(-U/T\right), \tag{5}$$

where ρ_{0f} is a prefactor term and is usually three decades higher than the normal resistivity, and U is the potential. In this model, U is presumed to be $U \propto H_c^2(t)\xi^n(t)$ [14], where n is the dimensionality of the vortex system, and $t = T/T_{\mathrm{c}}$ is the reduced temperature. Thermodynamic $H_{\mathrm{c}} \propto (1-t)$, and $\xi \propto (1-t)^{-\frac{1}{2}}$ [5], hence it is obtained $U = U_0(1-t)^q$, where $q = 2-n/2$ [13,15]. For YBCO q is 1, therefore $U = U_0(1-t)$. Thus, the activation energy U_0 can be estimated with an Arrhenius plot

$$\ln\rho = \ln\rho_0 - \frac{U_0}{T} = \ln\rho_{0f} + \frac{U_0}{T_{\mathrm{c}}} - \frac{U_0}{T}, \tag{6}$$

where $\ln\rho_0$ is the limit when $1/T \to 0$, and U_0 is the slope in the logarithmic vs $1/T$ plot and is considered temperature independent [16].

1.2 Pinning sites

1.2.1 Natural pinning sites

A superconducting material has usually a spectrum of defects which can act as pinning sites. Their strength depends on their geometry, and those which can trap the vortex at its whole length are considered strongest [5].

The linear defects such as screw dislocations are introduced in the thin film growth, and they act as strong pinning sites [11,17]. Because these dislocations evolve in growth island boundaries during the film preparation, they have nonrandom positions in the film. That is why they result in plastic pinning ($\alpha = -0.5$) instead of collective pinning ($\alpha = -1$) as in single crystals with randomly distributed correlated defects [17]. The high density of such pinning sites in thin films is one of the reasons why they are considered one of the most promising material for the coated conductor (CC) fabrication.

Twin boundaries form in ReBCO thin films on cubic substrates like STO, when the tetragonal ReBCO material undergoes a phase transition to orthorhombic as it is cooled at a sufficiently high oxygen pressure from above 500°C to the room temperature [18]. The nucleation of twin domains occur in separate islands, and as the temperature is reduced, the islands grow in size. The a (or b) ($a < b$) axis of a twinning island can

align either along a or b axis of the substrate, therefore the twin domains have a random alignment. As the perpendicularly aligned twin domains meet, a twin boundary is formed. The twin boundaries are rather strong pinning sites, since they are planar and can trap the vortex within its whole length, if F_{L} is perpendicular to the twin plane. In other geometries, the vortices may channel through the twin planes without pinning.

A stacking fault is an extra layer parallel to basal ab-plane [19]. Such an extra layer can be a Cu–O-layer in YBCO [19, 20] or a Gd-layer in GdBCO [21].

There are also a number of other lattice defects which can act as a pinning sites such as antiphase boundaries, mis-aligned grains, voids etc. A list of such a defects is given in reference [19] and [22].

A method to increase the number of the natural pinning sites is to use a target with nanograined material for pulsed laser deposition (PLD) [23–25]. It has been shown that the particle size is smaller in the plume and on the substrate, and hence the higher J_{c} than in conventional targets of micronsized grains is attributed to them. Furthermore, using a nanograined target material enables full relaxation of the orthorhombic stress at lower thin film thickness than with targets with micronsized grains [25, 26]. In ref. [26] it was speculated that the twin boundaries tend to form in growth island boundaries, but in ref [25] the transmission electron microscopy (TEM) did not support that. Hence the defects responsible for high J_{c} are some other correlated, linear defects, like dislocations.

1.2.2 Artificial pinning sites

There are additional methods to enhance pinning artificially. One possibility is to irradiate a superconducting thin film or a single crystal with light ions [27–29] or heavy ions [29, 30], where the light ones create point-like defects in the material and heavy ones correlated, strong pinning sites. A cheaper and more suitable way for large scale thin film manufacturing is the use of substrate with nanodots, such as Ag [31]. The nanodot does not allow stoichiometric, superconducting material to grow above it, and hence a correlated pinning site is formed. Yet another way to emerge columnar defects is to use miscut substrates in thin film growth [20]. In addition, the pinning properties can be improved by introducing precipitates inside the superconducting material. A such a method is the multilayering.

In multilayering, a non-superconducting layer is usually deposited inside the SC. The used materials are such as Y_2O_3 [32–34], CeO_2 [35–38], Y211 [39], YSZ [40], transition metals (Ti, Zr, Hf, Ir) [41, 42], and $BaZrO_3$(BZO) [43], and mixing supercon-

ducting materials like ReBCO (Re = Gd, Nd, Eu and Dy) [44,45], and even a ferromagnetic material [46]. The best enhancement has been achieved with quasi-layers, whose thickness does not allow forming of a complete layer. This will result in nanoparticulates or precipitates [32–34, 37, 39–41, 43]. The particulates themselves behave as pinning sites, but multilayering can also increase the amount of disorder [45] and stress [39] in the superconducting material. If complete or almost complete layers are formed, the superconducting properties do not enhance or they even decrease [32]. The critical temperature tends to decrease as the layer thickness increases [32,34,37,40–42], the same is seen for $J_{\mathrm{c}}(B = \text{self field})$, as well as widening of the transition [32, 34, 40]. In contrast to the former, Haugan *et al.* did not detect decrease of T_{c} and $J_{\mathrm{c}}(B = \text{self field})$ with BZO [43], the reason might be that they used a stoichiometric material, therefore the Zr and other transition metals do not poison the superconducting properties as it was the case of Hänisch *et al.* [41]. The enhancement of J_{c} in magnetic field was determined by the thickness of the non-superconducting material as well as by the thickness of superconducting material [39, 40]. In addition, the J_{c} improvement was more pronounced at low temperatures for multilayered films than for films without multilayering, in comparison to high temperatures, i.e. 77 K [37, 41, 43]. By varying these two thicknesses, a J_{c} enhancement can be achieved in the low, intermediate or high magnetic field range depending of the two thicknesses [32, 39, 41–43]. The situation is the same for multilayers consisting only of SC's: the enhancement of superconducting properties depends on the layer thicknesses [44]. Also, an improvement of the irreversibility field B_{irr} was seen for multilayering [34, 40]. A development of correlated pinning sites was seen for BZO (or YSZ), and Hf, which reduced anisotropy of J_{c} in the magnetic field rotation measurements [40, 41]. Instead Y_2O_3 improved the random pinning [33]. One of the advantages of multilayering is also the possibility to grow thicker films with an actual increase of critical current I_{c} [36].

Another way is to add precipitates in the target material directly. As in the multilayering case of transition metals, YSZ and BZO, the precipitates align along the c-axis introducing correlated strong pinning sites if ReBCO material is doped with BZO (or YSZ or ZrO_2, which both react with ReBCO material to form BZO) [25, 43, 47–55], Yb_3TaO_7, Gd_3TaO_7, YBa_2NbO_6 [56], or gold [57, 58]. Therefore, the angular dependence in magnetic field becomes more isotropic [47, 48, 52–54]. This is due to the wide c-axis peak which is concluded to originate from the correlated defects. Indeed, as in multilayering, the nanorod does not completely consist of BZO particles, but the spacing is filled with YBCO [59]. Increasing the BZO-doping decreases the T_{c} and J_{c}(0 T) [43,

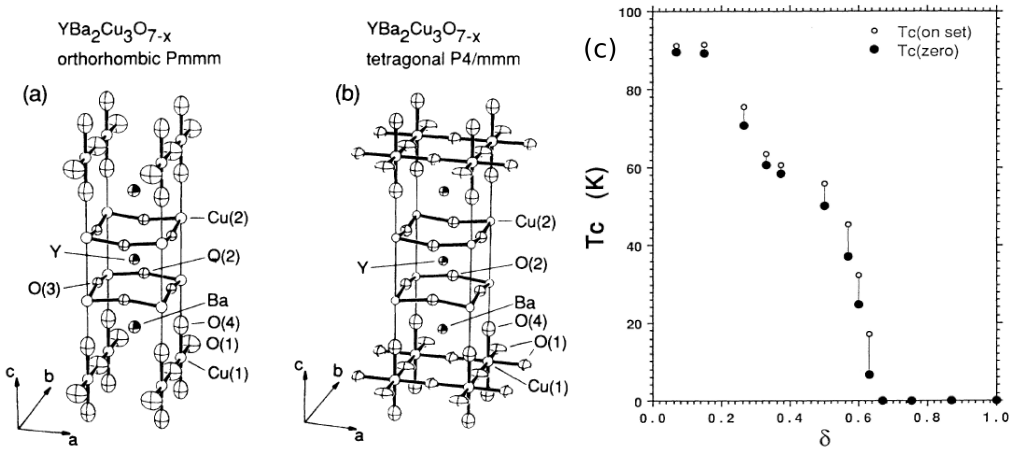

Figure 1. The orthorhombic (a) and tetragonal structure (b) of YBCO [61], and the T_{c} vs oxygen deficiency of a YBCO thin film (c) [62]

49]. However, an increase of J_{c} is seen at non-zero magnetic fields [47, 48, 52–54]. The doping level determines the field range where the J_{c} is improved, and an optimum is found with 3.9 wt% of BZO in YBCO [49]. The radius of a single BZO-nanorod does not grow with doping level, instead their number increases [49]. Furthermore, some additional dislocations are also found in vicinity of BZO nanorods, which probably increase the pinning [25]. The pinning potential, U_{p} is shown to increase with BZO-doping level [16]. Irreversibility temperature T_{irr} or field B_{irr} depends on the BZO-doping level as well, and hence the optimum level depends on the desired B_{irr}, a higher doping giving higher B_{irr}.

1.3 Structure of *RE*$\mathbf{Ba_2Cu_3O_{7-\delta}}$

The $Re\mathrm{Ba_2Cu_3O_{7-\delta}}$ (Re = Y, Pr, Nd, Sm, Eu, Gd, Ho ...) (ReBCO) group of material was initially found by Wu *et al.* in in 1987, as they investigated Y–Ba–Cu–O composition [60]. Later it was found that the actual superconducting compound was $\mathrm{YBa_2Cu_3O_{7-\delta}}$ (YBCO). Since then, almost all of the rare-earths have been swapped to the Y site. YBCO has a superconducting phase, if oxygen deficiency $\delta \leq 0.6$, and it has an orthorhombic $Pmmm$ structure (figure 1(a)) [61]. With lower oxygen contents, the structure becomes tetragonal $P4/mmm$ (figure 1(b)) and non-superconducting.

The behaviour of the T_{c} is presented in figure 1(c) for thin films. This peculiar dependence of T_{c} on δ, i.e. the three plateaus, has been explained by reducing oxygen

deficiency destroying holes [61, 63, 64], which act as charge carriers of superconductivity. The ordering of the oxygen in basal planes, i.e. Cu(1)–O(1)-planes, is also shown to form oxygen or vacancy chains, an ordered alternating oxygen–vacancy lattice [65].

1.4 $YBa_2Cu_3O_{7-\delta}$ vs. $GdBa_2Cu_3O_{7-\delta}$

The unit cell and the structure are the same for YBCO and $GdBa_2Cu_3O_{7-\delta}$ (GdBCO), only the ionic radius is different: 1.019 Å for Y^{3+} and 1.053 for Gd^{3+} [66]. This results in an easier cation disorder for Gd and Ba than for Y and Ba, because the radius of Gd^{3+} is closer to $Ba^{2+}(= 1.35$ Å) [67] than to Y^{3+}. This results also in a slightly higher stability for YBCO than GdBCO, since a smaller cation radius results in higher stability [66, 68]. The lattice parameters have also minor differences. For YBCO the lattice parameters are: $a = 3.817$ Å, $b = 3.883$ Å, and $c = 11.633$ Å, and for GdBCO: $a = 3.859$ Å, $b = 3.885$ Å, and $c = 11.759$ Å [69]. However, T_c does not depend heavily on the rare-earth [70] (only Pr and Ce result in a non-superconducting ReBCO phase), and that is one of the reasons why the superconductivity is attributed to the CuO-layers. For thin films, the T_c is slightly higher for GdBCO than YBCO [71–74]. That might be a reason why the J_c and B_{irr} are higher for GdBCO than for YBCO at 77 K [52–54, 73, 74,]. The higher J_c and B_{irr} are also suggested to originate from extra defects, which Takahashi *et al.* were not able to identify in ref. [75], but in subsequent publications they identified extra stacking faults [52, 53], which was confirmed by Haberkorn *et al.* [21]. The latter group also identified a stacking fault as an extra Gd-layer, which agrees well with the cation disorder. Some screw dislocations are also found in GdBCO, but their number is lower than in YBCO [74]. Due to the defects, GdBCO is also shown to have more isotropic magnetic field angle dependence of J_c [52–55, 74, 76]. In addition, the volume of a-oriented grains does not grow as fast with the increasing film thickness as in YBCO in conventional film growth processes, causing much smaller degradation of J_c for thicker films, and hence the critical current increases faster in GdBCO [53, 54, 76]. GdBCO has been also successfully grown with an in-plume-PLD method, allowing up to three times faster film growth with improved transmission properties [77, 78]. The drawback of the GdBCO thin films is the observed aging effect, which reduces the J_c with time [79].

1.5 Motivation

The pinning properties determines the superconducting properties of the material even more than T_c. Therefore, pinning in high temperature superconductor (HTS) material

has been under heavy investigation after their discovery. Recently, it was shown in our group, that ablating thin films from the nanosized target material has enhanced the pinning of YBCO [25, 51]. To strengthen this argument, a series of YBCO targets of different densities were made and studied in paper [**P2**].

To enhance the pinning properties of YBCO and in order to find the best pinning properties possible to achieve by BZO-multilayering, a set of different multilayers and nanorod-type BZO was grown inside the YBCO in paper [**P3**]. The growth mechanism was also investigated.

As it has been shown previously, the substitution of Y by Gd has increased the pinning properties of YBCO structured HTS materials. In addition, as mentioned above, a higher J_c has been achieved in YBCO by using a target material of nanosized grains. Therefore, GdBCO thin films were deposited from a nanograined target material. To further increase the pinning properties of ReBCO material, GdBCO was doped with 4 wt% of BZO which is known to be the optimal doping level in YBCO. To investigate the pinning properties of GdBCO, the structural and superconducting property study was made in paper [**P1**], and the work was continued with resistivity measurements in paper [**P5**].

An aging effect has been discovered in GdBCO [79], but it has not been systematically studied. To find out the origin and the nature of the aging, a systematic magnetisation and structure investigation was made in paper [**P4**].

2 Experimental details

2.1 Sample preparation

All the precursor powders, which are the initial target materials, are made by the sol-gel method. At the starting point, all the materials are nitrate salts in water solution. The precise molar amount of each component, Y or Gd, Ba, and Cu, are mixed together. The citric acid is added so that the pH of the solution is 5. Then, the solution is dried in 80–90°C for 20 hours or until it gradually has formed a gel. The dried powder is slightly ground, and then calcinated first at 500°C for 20 min, then at 725°C for 2 hours. This step is often repeated to ensure the purity of the material [**P2**]. On the other hand, this step has been also done in a slightly different way, where powders are either calcinated at 790°C for 14 hours or at 780°C for 96 hours, after that the powder is slightly ground and deoxydised in flowing Ar in 100 kPa at 750°C for 24 h, and then cooled down to 400°C in oxygen atmosphere where it is annealed for 4 h [80]. In each of these routes, nanosized grain-size is retained as well as the phase purity. The purity and grain-size of the precursor powder were checked with x-ray diffraction (XRD) by $\theta-2\theta$-scan. For GdBCO, the route is basically the same but some adjustments are needed: e.g. temperatures and treating times have to be modified. For BZO-doped materials, the exact wt% of starting material, that is Ba and Zr, are added to starting solution, and the targets are treated similarly as the undoped ones. The precursor powders are pressed into pellets at ≈340 MPa, then sintered at 900°C for a short while. The YBCO targets in [**P2**], T1–T4, were sintered at 850°C–900°C for 15 min, to get different target densities. The undoped and BZO-doped GdBCO targets were sintered at 900°C in oxygen flow for five hours. A subsequent long term oxygen treatment was sometimes needed to get the orthorhombic phase of the target material.

A pulsed laser deposition (PLD) method was used for thin film growth. The laser was XeCl ($\lambda = 308$ nm) excimer type. $SrTiO_3$ (STO) (100) single crystals were used as film growth substrates. The substrate temperature, T_s, was varied between 625°C–765°C for the growth condition optimisation for GdBCO, and the optimum was found at 700°C, whereas the optimum was 745°C–780°C for undoped and BZO-doped YBCO. The pressure in the chamber was 300 mTorr of flowing oxygen during each ablation. Energy densities of 1.8 J/cm^2–2.1 J/cm^2 and in-axis geometry were used so that the tip of the plume just reached the substrate, when substrate-target distance was 35 mm. The single layered (in contrast to multilayered) films were fabricated without a change of target, and 1500 or 1800 pulses were always shot, if not otherwise mentioned, with

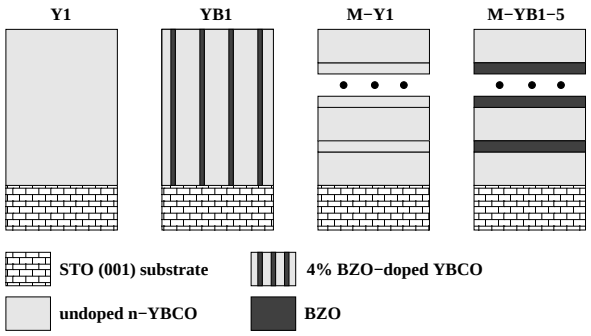

Figure 2. Types of multilayer structures k x [YBCO(m pulses)/BZO(n pulses)] used in [**P3**]. Layer thicknesses of YBCO (m) and BZO (n) and number of bilayers k vary in structures M-YB1-5 as mentioned in the text. The single-element multilayer 20 x [YBCO(100 pulses)/YBCO(20 pulses)] (M-Y1) as well as the conventional undoped nanostructured YBCO (Y1) and 4% BZO-doped YBCO (YB1) films were made for comparison. [**P3**]

repetition rate of 5 Hz, and the calibrated film growth rate was 1 Å/pulse, resulting in 150–180 nm thick films depending of pulse number and growth conditions. This thickness was enough to produce structurally fully relaxed films [25]. For the multilayered film study, 2400 pulses were shot for each film, in order to get the same film thicknesses. $k \times [\mathrm{YBCO}(m \text{ pulses})/\mathrm{BZO}(n \text{ pulses})]$ multilayers were deposited in the same, optimised conditions, only the pulse numbers $m = 50 - 2400$ and $n = 0 - 50$ as well as the layer number $k = 1 - 40$ were varied, see table 3 on page 19 and figure 2. All the films were oxygen treated *in situ* slightly below T_s in 1 atm oxygen pressure for ten minutes, after that the thin films were slowly cooled to an ambient temperature.

For aging investigations, a GdBCO and an YBCO thin film were made with PLD. Both the films were split, and one half was gold-coated (Au-GdBCO and Au-YBCO) whereas the other half was left without coating (uc-GdBCO and uc-YBCO). The Au-coating was made by sputtering at the room temperature, and the thickness of the Au-cap layer for the Au-YBCO was 50 nm, and a thicker layer, 100 nm, was sputtered onto the Au-GdBCO film to compensate for the higher surface roughness. Both the films were kept in ambient air, and x-ray diffraction and magnetisation measurements were made at one month intervals for five months. In addition, an uncoated GdBCO film was made for x-ray photoelectron spectroscopy (XPS) studies which were made for a fresh and a seven months old film.

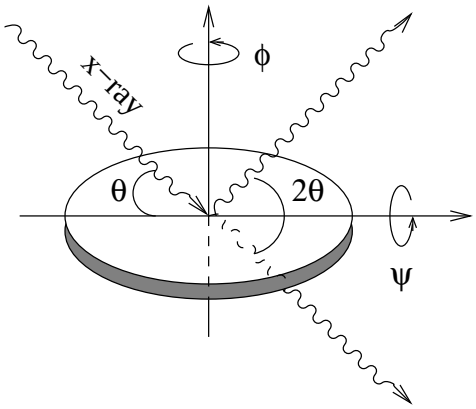

Figure 3. A schematic illustration of Bragg-angle θ, tilt angle ψ, and rotation angle ϕ.

For resistivity measurements, a 50 μm wide pattern was etched for the four-point measurements: the patterns were made by the photolithography, and the extra material was removed with phosphorus acid. The soldering was done by mechanically tapping indium onto the contact pads.

2.2 Characterisation methods

2.2.1 X-ray diffraction

The structural characterisation of the films was made by XRD measurements using Philips X'Pert Pro diffractometer with Schultz goniometer. The used radiation was Kα-line of copper. A Ni filter was placed into incident beam optics to reduce the intensity of CuKβ-peaks, and a parallel plate collimator, and a 0.18° entrance slit were added into diffracted beam optics. Also, 0.04 rad Soller-slits were inserted into both beams. For powder diffraction, 0.5° anti-scatter slits and 0.04 rad Soller-slits for incident and diffracted beams, and for diffracted beam, a crystal monochromator with 0.3 mm aperture were used.

To check the phase purity of the thin films, $\theta - 2\theta$-scans in (00l) direction were made. The texture of the films was studied at $2\theta = 27.8°$, corresponding the (102)-peak of YBCO and GdBCO and at $2\theta = 30.8°$, corresponding the (110)-peak of BZO.

The twin structure of the films was checked from the (212)/(122)-peaks, which are in vicinity of $(2\theta, \psi, \phi) = (56.0°, 73.0°, 26.5°)$, where θ is the Bragg angle, ψ is the tilt angle and ϕ is the rotation angle (figure 3). The volume of a-oriented grains was determined from intensity ratios of a- and c-axis oriented (102)-peaks, where the

$(27.7°, 56.7°, 0°)$ corresponds to the c-oriented grains and $(27.7°, 33.3°, 0°)$ the a-oriented grains. Hence the peaks have well separated ψ-angles. The ratio is defined as $I_a/(I_a + I_c)$, where I is the geometry corrected intensity of a respective peak.

The geometry correction, which can be done either by adjusting the receiving slits or by mathematical calculations, is needed in the intensities, if the peaks have different tilting angles, ψ's [81]. As ψ increases, the diffracted intensity fitting inside the receiving slits reduces, because the intersection of the sample surface and the beam changes its shape and orientation. Also, in the case of a thin film, the tilt increases absorption, but whereas in a thick slab the decrease of absorbing volume compensates the increased intensity, in thin films the x-rays easily penetrate the whole sample at any tilts (since penetration depth of x-rays may be up to 100–200 μm and the thickness of a thin film is only hundreds of nanometres) [81, p. 143–147]. This change of the intensity can be calculated or empirically determined [81, p. 143–147]

2.2.2 Magnetisation measurements

The superconducting properties of the films were determined with magnetisation measurements which were made with Quantum Design Physical Properties Measurement System (PPMS). The magnetic field was always applied along the c-axis and perpendicular to the film surface. The onset value of T_c was determined from the real part of ac-magnetisation, where frequency (113 Hz) not commensurable with 50 Hz of mains current, and ac-field of 1 mT was applied without any external dc-field.

dc-magnetisation hysteresis loops were measured in a field range of $-8\ \mathrm{T} \leq B \leq 8\ \mathrm{T}$. From the obtained loops, the critical current, J_c, was estimated with Bean model [82–84]:

$$J_\mathrm{c} = \frac{\Delta m_\mathrm{irr}(B_\pm)}{a(1 - a/(3b))V}, \tag{7}$$

where a and b ($a \geq b$) are the length and width of the rectangular film, V is the volume and $\Delta m_\mathrm{irr}(B_\pm)$ is a half of the opening of the hysteresis curve that is $2\Delta m\mathrm{irr} = |m(B_+) - m(B_-)|$. The J_c is presumed field independent in Bean model [82, 83], but still it gives a good estimation [85]. However, it has to be pointed out that the J_c obtained with a magnetisation method should not be compared with J_c's obtained with transport measurements, since the magnetisation gives an average over the whole film, the transport measurements give the J_c from a small part and its voltage criterion (the voltage which indicates normal state resistivity) is different [85].

2.2.3 Atomic force microscopy

The surface morphology of a sample was determined by an atomic force microscope (AFM), ParkScientific AutoProbe AFM/EFM/STM/MFM. In this work, the so called contact mode was always used, which means that the tip of AFM touches the sample, and a given, constant force (50 pN) is maintained as the tip is swept on the sample. The root-mean-square-roughnesses (rms-roughnesses) are calculated from areas of given size, and only the rms-roughnesses of the same, given size are compared. For film thickness, a step or a 50 μm wide stripe was etched, and its height was measured with AFM. Also, for resistivity measurements, the actual width and height of the stripe was measured by AFM.

2.2.4 X-ray photoelectron spectroscopy

The x-ray photoelectron spectroscopy (XPS) measurements were carried out by Dr. Sari Granroth in Materials Research Laboratory in University of Turku. The XPS spectra were collected by Perkin-Elmer PHI 5400 spectrometer using Mg Kα radiation (1253.6 eV). The pass energy of the analyser of 89.45 eV, and take-off angle of 45° were applied for core-lever spectra measurements. The base pressure was around $2 \cdot 10^{-9}$ Torr during the measurements. The binding energy (BE) scale calibration was made by using the C $1s$ core-level in the thin film sample and the standard Au $4f_{7/2}$ (BE=83.98 eV) reference line.

2.2.5 Resistivity measurements

The resistivity measurements were made with the PPMS. The applied current was 10 μA in the results presented in [**P5**], although lower currents were also investigated. The resistivity versus temperature, $\rho(T)$, measurements were started at 110 K, and the temperature was slowly reduced, 1 K/min above the transition, 0.2 K/min in the vicinity of the transition, and 1 K/min below the transition until the measurement was ended well below the transition at 50 K. The $\rho(T)$ curves were obtained at magnetic fields of 0, 0.1, 0.5, 1...8 T, in both, parallel and perpendicular directions with respect to c-axis. The magnetic field was always perpendicular to the current i.e. the maximum Lorentz force configuration.

The resistivity versus rotation angle in an external magnetic field, $\rho(\Theta)$, were measured at constant fields (0.5, 0.75, and 1 T) and constant temperatures. The maximum Lorentz force configuration was again used.

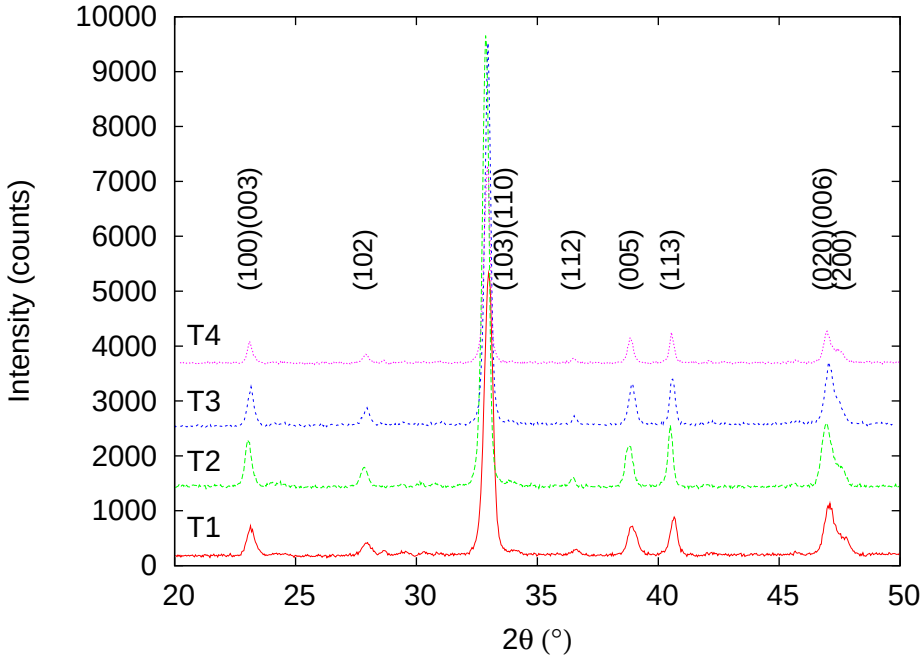

Figure 4. The XRD 2θ-scans of the T1–4 targets. [**P2**]

3 Results and discussions

3.1 Influence of target density

The XRD-patterns of four YBCO targets prepared at different temperatures are shown in figure 4. Some minor wiggling can be seen near 30° in T1 and T2 indicating some impurity phases, but the peaks are too small for identification, and therefore the targets are practically phase pure. Furthermore, since the targets are made from the same source powder, these impurities should not influence the film properties. The similar peak widths indicate similar grain size in the targets, and moreover, a careful grain-size analysis with the Rietveld refinement indicates also only small variation of 25–45 nm (table 1). The target grain size grows from T1 to T4, but it is not expected that such a small variation affects the film properties, although the grain size has been shown to influence the film properties [12, 86, 87], but in those cases the grain size difference was wider: micrometres vs. nanometres. The sintering temperatures 850°C and 875°C did not result in much target density increase, but above a threshold temperature, the density grows fast. Our results indicate, that 15 min at 900°C in air was enough for the target to became denser without a significant grain size growth. The sintering was done also

Table 1. Properties of the targets. The relative density is calculated from the theoretical density of 6.375 g/cm^3. [**P2**]

Target	T1	T2	T3	T4
Sintering temperature (°C)	850	875	887	900
Target grain size (nm)	25	36	39	43
Target density (g/cm^3)	4.1	4.1	4.3	5.0
Relative density (%)	63.5	63.8	66.9	78.6
Polishability (%)	21.7	22.9	31.3	61.3

below 850°C and above 900°C, but the results did not differ from the data presented herein. This agrees with previous sintering studies [88, 89]. The sintering of the targets in oxygen atmosphere was also tried, and pure YBCO was achieved, but the sintering time for denser targets were much longer than in air. The sintering in Ar resulted in several impurity phases i.e. $BaCuO_2$, Y_2O_3 and CuO in the target, which is in accordance with the measured phase diagrams [90].

The maximum obtained density for the nanograined target (T4) was approximately 80% of theoretical value. It is clearly less than the density of targets of larger grains, but the value agrees well with value of very fine powders [88]. On the other hand, sanding of the nanograined targets is harder: although the less dense targets, T1–T3, were more powder-like than T4 whose density is 80%, their sanding felt the same as for microngrained target whose density is about 90%. To quantify this, all four targets were sanded with sanding papers graded 240, 800, and 1200 in respective order for the same amount of time. Then, the proportion of the shining area of the targets were measured with optical microscopy. This is called a polishability, and it is included in table 1. Since the grains are more attached to the denser targets, less grains are detached during the sanding, and only on the attached grains a reflecting surface is polished. The surface of the targets was also imaged after the laser ablation with optical microscopy. Since a wavy pattern, with size of 20 μm was seen, and since it is typical of target surfaces shot with similar laser fluency [91, p. 97], the surface feature did not depend on the target density.

Table 2. Structural and superconducting properties of the films [**P2**].

Sample	F1	F2	F3	F4
T_c(K)	88.5	88.7	88.3	89.3
J_c(10 K, 0 T) (MA/cm^2)	39.2	32.0	22.2	29.9
B^* (10K) (mT)	64.7	60.7	108.5	75.9
Thickness (nm)	153	150	160	152
rms roughness (nm)	3.95	3.96	3.36	2.68
$I(005)/I(004)$	11.9	11.1	12.9	11.1
FWHM (005) ($^\circ$)	0.320	0.313	0.333	0.324
$\Delta\omega$ ($^\circ$)	0.242	0.222	0.255	0.240
r_c (nm)	17.6	19.2	16.7	17.7

3.2 Surface roughness

The surface roughnesses of the films were measured with AFM. The results of the films, F1–F4, made from targets with different densities, T1-T4, (see section 3.1) are shown in the table 2; the roughnesses were calculated from measured areas of 2, 5 and 10 μm^2 by taking an average. The roughnesses of these films is clearly smaller than the on-axis made films from micronsized targets of any density [92–94]. This can be explained by the nanosized grains in the target [87]. The film roughnesses in our films depend on the target density, as it can be seen in table 2. This agrees with the earlier results, where targets of tetragonal and orthogonal phase are compared [92, 95], and the smoother surface of a tetragonal phase is explained by its higher density.

The results for surface roughnesses of undoped and optimally BZO-doped single layered YBCO (Y1 and YB1, respectively) as well as multilayered YBCO/BZO films (M-Y1, M-YB1–M-YB5) are shown in table 3. The roughness of the single layered, undoped YBCO film is two times higher than that of the conventionally BZO-doped YBCO film, YB1. This can be explained by the partial change of the growth mechanism [96]. The undoped YBCO grows as the island type, but introducing of BZO inclusions results in a more two dimensional type of growth. This is probably due to increased mobility of adsorbed atoms, which leads to smoother surfaces [93].

The rms-roughnesses of undoped and BZO-doped GdBCO films were 5–10 nm as measured from 5×5 μm^2 areas. These roughnesses are higher than in YBCO films made from T1-T4 targets (table 1), and undoped YBCO film, Y1, and BZO-doped YBCO,

YB1, also they are higher than the values found in literature for GdBCO [87, 97]. The BZO-doped GdBCO had higher roughnesses than undoped one, and this is in contradiction with the lower roughness of YB1 than Y1 (table 3). However, BZO-doped GdBCO target was far less dense (4.1 g/cm^3, $\approx$ 60%) in comparison to undoped one (5.5 g/cm^3, $\approx$ 80%), and therefore the density difference, which is discussed above, explains the contradiction. Nevertheless, the surface morphology of GdBCO based films is slightly rougher than that of the YBCO films.

The single element multilayered YBCO, M-Y1, shows higher roughness than the single layered pure YBCO, Y1 (see table 3). This can be explained by the increased vertical alignment of particles because of relatively long holding time between the layers, and therefore the basic units have more time to move to the energetically more favourable sites [39, 98]. On the contrary, in YBCO/BZO multilayers, M-Y1–M-Y4, the surface roughness is smaller than in single layered one, and it is in 2–3 nm range, and in M-Y5 the roughness is 4.7 nm (table 3). The results show that if the YBCO layer is thin enough, the surface is very smooth and does not depend much on the BZO layer thickness. A similar effect has been seen earlier [44, 99]. This can be explained by development of planar and linear defects as well as edge dislocations at the multilayer interface boundaries [45, 99]. These defects compensates the mismatch of YBCO and BZO layers and therefore release the strain producing smooth surfaces. In multilayer M-YB5, the both YBCO and BZO layers are thicker than in the other multilayers and that is why they grow in a island mode like structure, which results in surface roughening. This phenomenon is well described in literature [39, 100, 101].

Table 3. The number of pulses of the YBCO layer m and the BZO layer n, as well as number of bilayers k in single element and multilayers of k x [YBCO(m pulses)/BZO(n pulses)] and structural properties measured by AFM and XRD. [**P3**]

Sample	Y1	YB1	M-Y1	M-YB1	M-YB2	M-YB3	M-YB4	M-YB5
m	2400	2400	2400	100	100	100	50	250
n	0	0	0	20	5	3	2	50
k	1	1	1	20	20	20	40	8
Roughness (nm)	6.5	3.5	7.3	2.5	2.2	2.7	2.6	4.7
YBCO c-axis								
Peak 1 (nm)	1.163	1.171	1.165	1.175(48)	1.167(54)	1.166(96)	1.168(99)	1.166(85)
Peak 2 (nm)				1.161(48)	1.162(44)	1.143(2)	1.202(1)	1.165(13)
Peak 3 (nm)				1.200(4)	1.199(2)	1.193(2)		1.205(1)
Peak 4 (nm)								1.223(1)
BZO (110)								
FWHM (°)		1.304		1.443	1.713	1.920	1.705	0.992
Rocking curve								
YBCO (005)								
FWHM (°)	0.214	0.247	0.292	0.882	0.357	0.340	0.325	0.630
r_c (nm)	19.873	17.243	14.563	4.834	11.936	12.528	13.098	6.759
BZO (002)								
FWHM (°)		0.305		0.567	0.414	0.377	0.379	0.704
r_c (nm)		12.500		6.724	9.209	10.113	10.059	5.415

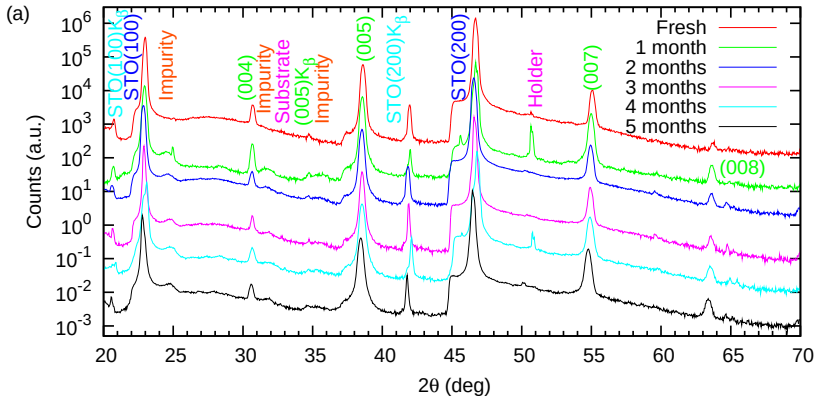

Figure 5. The 2θ-scan of Au-GdBCO. A development of some impurities can be seen with time. [**P4**]

3.3 Film structure

3.3.1 Phase purity

The phase purity of the films was checked with $\theta - 2\theta$-scans (Bragg–Brentano-scans) of $(00l)$-peaks that is the direction perpendicular to the film plane. An example of such a measurement is shown in figure 5. None of the films except the gold-coated GdBCO, Au-GdBCO, showed impurity peaks at any point in the analysis. The fresh Au-GdBCO did not show any impurities either, but some minor impurity phases developed with time (figure 5).

3.3.2 *a*/*c*-oriented grain fraction

The volume of a-oriented grains was determined from (102)-peak, which has a clear separation of the a- and c-orientation in ψ-angles as discussed above in the section 2.1. All the YBCO films in this work had the a-oriented grain volume less than 1%. This is in accordance with earlier results, where it was suggested that a-oriented grains grow in the substrate–film interface, because the substrate surface has a lower temperature in the beginning of the deposition due to the higher emissivity of a clean substrate in comparison to an ablated substrate [26, 102]. In multilayers, YBCO grows practically completely c-oriented on BZO layers, too. The GdBCO films have higher volume of a-oriented grains than YBCO films, that is 3–4 %. In comparison to coated conductor films, our films had slightly more a-oriented grains [53,54] and less or similar amount in

comparison to films on single crystal substrates [73,97,103,104]. Of course, some of this amount is also due to the lower substrate temperature in the beginning of the deposition. However, the relatively thin GdBCO films have more a-oriented grains than YBCO. The difference can be qualitatively explained by longer c-axis parameter of GdBCO than YBCO [69], which results c parameter to be closer to triple value of lattice parameter of STO. This would lead to lower strain of the lattice, and the correctly grown lattice would not be as much energetically favourable in GdBCO as in YBCO. Furthermore, the optimum T_{s} is 50°C lower for GdBCO than for YBCO, which can also explain the higher volume.

The a-oriented phase is stable, it was seen that its volume does not grow with time in GdBCO within eight months, which was expected.

3.3.3 Twinning and in-plane structure

The twinning and in-plane structure was studied by two dimensional XRD $(2\theta, \phi)$-scans. For all the single layered, undoped YBCO, a typical twinning with ϕ-split of 0.9° was always found (figure 6). Similar structure was found for undoped GdBCO as well. This kind of four peak system (inset of figure 6) has been seen in YBCO earlier, where the ϕ-splitting was attributed to twinning [26, 105, 106], and it occurs in films grown e.g. on cubic substrates like STO to release the strain produced by orthorhombic relaxation (see section 1.2.1 for more details). Adding BZO-nanoparticles and -nanorods has been shown to decrease the ϕ-split [49] but to increase the FWHM of the peaks, indicating increased stress [25, 26], which points to an influence on a relaxation of strains caused by the transition from tetragonal to orthorhombic. The BZO-doping causes more severe decrease of the ϕ-split and also a widening of the (212)-peaks in GdBCO than in YBCO, therefore a similar, 4 wt%, BZO-doping has more effect on GdBCO. The situation is partly different in YBCO/BZO-multilayers since thick enough, 20 nm or more, BZO layers (M-YB1 and M-YB5) result in a completely merged, broad peak (figure 6). A similar phenomenon has been seen in YBCO grown on MgO substrate, where a rather large lattice mismatch causes low-angle grain boundaries and other crystalline defects [105, 107].

There is no major change in (212)/(122) peak separation and width in any of the measured samples with time, but in careful two dimensional Gaussian peak fits described in more detail for undoped and BZO-doped YBCO [26], a small narrowing of the peaks is seen in GdBCO with time. This probably originates from the relaxation of the stresses by oxygen release that is discussed in more detail in section 3.3.5 and 3.3.6.

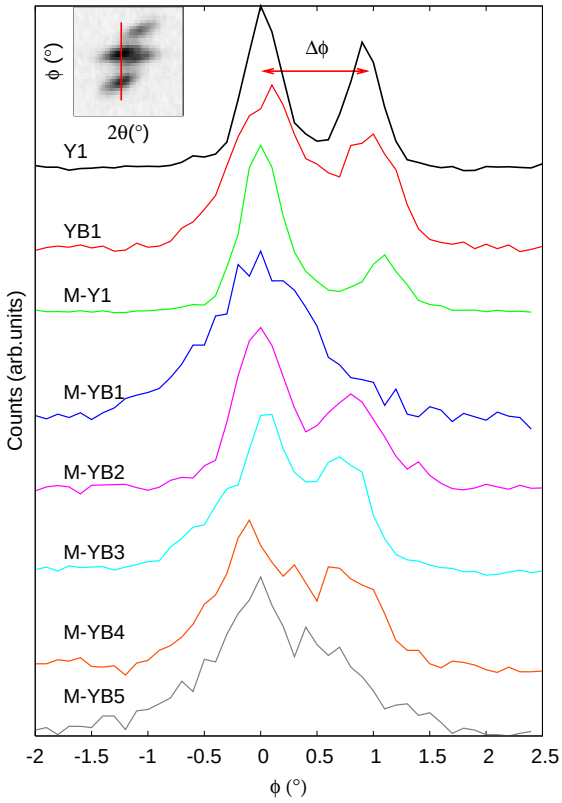

Figure 6. Lineplots in ϕ-direction over the (122) peaks for all single and multilayer structures. $\Delta\phi$ is the angle between the maxima of the peaks related to peak splitting due to twinning. The inset on left upper corner shows the whole (212)/(122) peak set for sample Y1. [**P3**]

3.3.4 Texture

The texture of undoped and BZO-doped single layered YBCO and GdBCO thin films was investigated by scanning the (102) peak over ψ and ϕ, where $\Delta\psi = \Delta\phi = 3^\circ$ (figure 7). The results show that undoped and BZO-doped GdBCO are well textured, similar to respective YBCO films (not shown). The texture measurement of BZO (110)-peak (inset of figure 8) shows that BZO has been well textured inside the GdBCO material and the $\theta - 2\theta$-scan of that peak (figure 8) indicates that BZO grows perpendicular to the film plane. Hence, the BZO grows cube-on-cube inside the GdBCO material. Earlier, it has been shown in our group for YBCO that textured BZO grows in nanorods [25, 108], and in literature, for GdBCO that BZO grows in nanorods [52, 53, 55]. Thus, the BZO

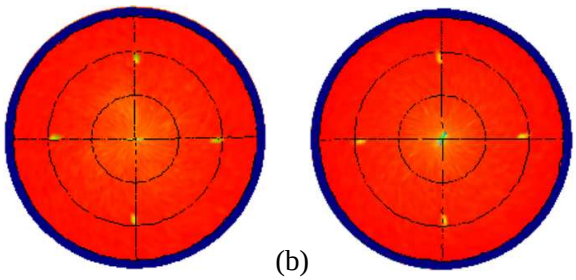

Figure 7. XRD pole figures of the GdBCO (102) peak where distance from the origin is the tilt angle ψ and the polar angle is ϕ. Undoped GdBCO (a) and BZO-doped GdBCO (b) films are well textured. [**P1**]

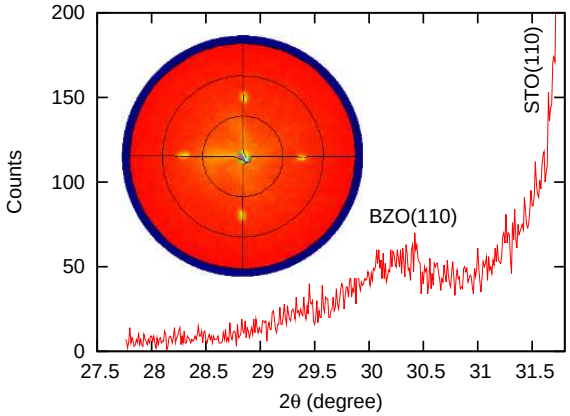

Figure 8. 2θ-scan of BZO doped GdBCO film. (110)-peak at (ψ, ϕ)=$(45°, 0°)$ shows that dopant grows cube-on-cube in GdBCO. The inset shows the pole figure of the BZO (110) peak. [**P1**]

grows most probably as nanorods in our GdBCO thin films, too, even though no TEM data are available for our samples. Also, the magnetisation measurements (see section 3.4.3 on page 33) confirm this.

3.3.5 Lattice parameter *c*

The lattice parameter c was calculated from (005) peak in the case of multilayer films, Y1, YB1, M-Y1, and M-YB1–M-YB5 (table 3 on page 19) from (004) and (005)-peaks in case of the films made from targets of different densities F1–F4 (table 2 on page 17), and for uc-YBCO, Au-YBCO, uc-GdBCO and Au-GdBCO (figure 9), by fitting

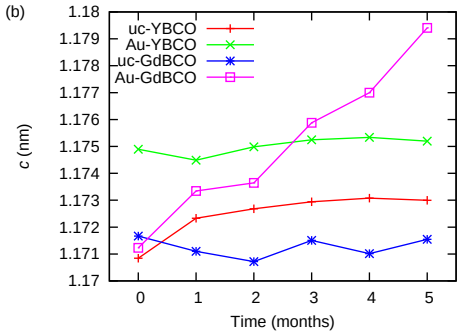

Figure 9. The development of the lattice parameter c with time. [**P4**]

the Bragg equation

$$2d \sin 2\theta = n\lambda, \tag{8}$$

where d is the spacing of the planes, θ is the Bragg-angle, n is the order of the reflection and $\lambda = 1.54178$ Å is the wavelength for CuKα. The lattice parameter of films F1–F4 is 1.168 nm, and it is a little bit higher than for Y1 (1.163 nm), but lower than for uc-YBCO (1.175 nm), though all these values are close to the lattice parameter of bulks (1.167 nm) [61]. There are many reasons where these differences may originate. First is the difference of the methods (one peak vs several peaks) where the calculation made from several peaks allows an elimination of some error parameters [109, p. 359]. Second is the misalignment of the instrument which is the most important factor if determining the lattice parameters [109, p. 359], and which is very difficult to keep equivalent for such a long period of time in which these measurements were done. Thirdly, the lattice parameters depend on the oxygen content, growth conditions such as substrate temperature, substrate material, and total and partial oxygen pressure during the deposition, and further on the crystal defects [62]. Indeed, the T_c (figure 13 on page 31) of Y1 is higher than the T_c of F1–F2 (table 2 on page 17) indicating a better oxygen content [61, 62] which will lead to a shorter c-parameter [62], although the origin of both might be the difference in structural defects, too. However, because the uc- and Au-YBCO as well as uc- and Au-GdBCO are split from the same original films, the longer c-parameter of Au-layered films (figure 9) indicates oxygen release or creation of defects during sputtering; though the change in oxygen content is probably the reason for this as discussed in the section 3.3.6, and further, there is no significant change in disorder as seen from (212)/(122) peak widths as mentioned in the section 3.3.3. The lattice parameter c grows with time in Au-GdBCO, whereas for rest of the films

it remains constant (figure 9), which can be explained by change of oxygen content or number of crystal defects, but as in the previous case, the oxygen deficiency is a more probable explanation.

Where all the single layered films showed only narrow single peaks, the multilayering (M-YB1–M-YB5) broadened and made the peaks asymmetric, and several separate peaks could be fitted to a peak complex. The c-parameters of the fitted Gaussian curves (with percentage shown in parenthesis) are given in table 3 on page 19. The columnar defects, or nanorods, lengthen the c-parameter, which can be related to the ordered structure of the strain and dislocation observed previously [25, 49]. In the multilayers where the thickness of the BZO layers is rather large in comparison to the YBCO layers (M-YB1 and M-YB2), a clear additional peak is seen. This peak has shifted to a lower angle, which indicates a phase with a longer c-parameter. The c-parameter reduces as the BZO layer thickness decreases, and this can be attributed to the lowered stress in BZO–YBCO boundaries of thinner BZO-layers. In M-YB5, the YBCO layer is relatively thick, and the two lattice parameters are close to the theoretical one.

3.3.6 Peak intensity ratios for oxygen content determination

As stated above, the length of lattice parameter c does not directly indicate the oxygen content of a thin film. However, Ye *et al.* in [62] discovered that the the intensity ratios of $(00l)$-peaks depend only weekly on the factors disturbing the c-parameter discussed above. Therefore, the intensity ratios can be used for an absolute oxygen content estimation for YBCO. The intensity ratio of (005) and (004) should be well below 20 and the $I(005)/I(007)$ above 5.5 in order to have oxygen deficiency $\delta < 0.1$ in YBCO [62]. However, cation substitution will reduce $I(005)/I(004)$ intensity [110, 111], so the ratio should be also above 12.5 to have cation substitution less than 2 %. The first rule is fulfilled for all the YBCO films (< 16 for multilayer films, see also table 2, p. 17 and figures 10 and 11). The F1–F4 films do not fit in the second boundary, therefore a slight cation substitution may have occurred in all these four films. The possible cation substitution should not have an effect on the magnetisation results, since the ratio is almost the same for all these four films (table 2, p. 17). The low $I(005)/I(004)$-ratio of the multilayer films indicate that the variation of the c-parameters does not result from the reduced oxygen content but the stress in BZO–YBCO interfaces as discussed in the previous section.

The oxygen content does not seem to change in YBCO samples with time, but in uc-GdBCO films there is a clear abrupt change between the intensity ratio measure-

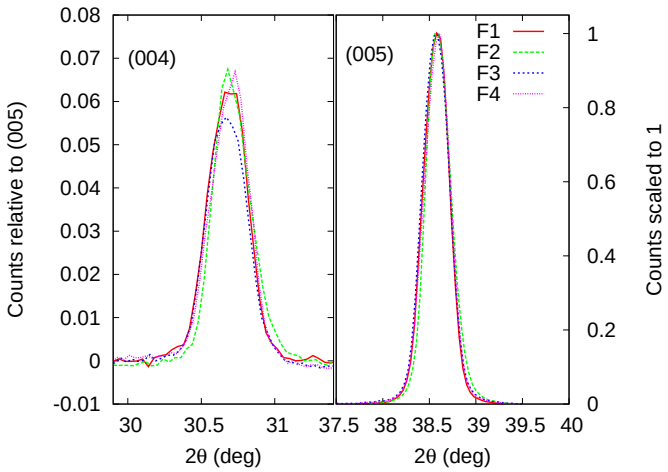

Figure 10. The XRD $\theta - 2\theta$ scans of (004) and (005) peaks of the films F1-F4. The intensities of the (005) peaks are scaled to 1 and the intensities of the (004) peaks are scaled with the intensity of the respective (005) peak . [**P2**]

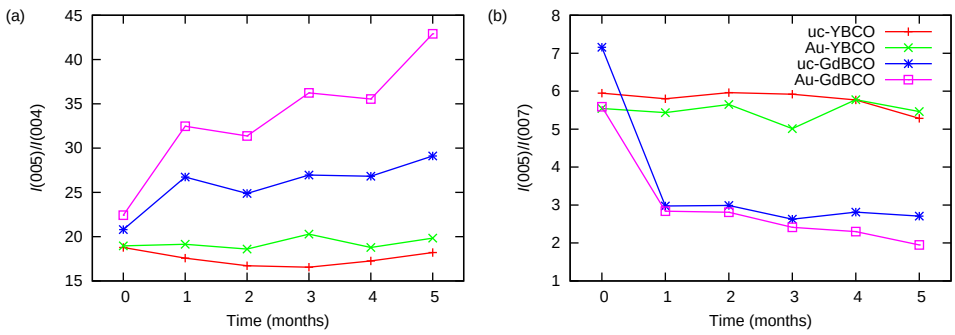

Figure 11. The time dependence of (a) $I(005)/I(004)$-ratio and (b) $I(005)/I(007)$-ratio. [**P4**]

Table 4. The lattice parameters and $I(005)/I(00l)$ intensity ratios for YBCO and GdBCO. The (Y⇔Gd) indicates the substitution of Y with Gd for calculations, and (Gd⇔Y) respective substitution for Gd.

	YBCO	GdBCO	(Y⇔Gd)BCO	(Gd⇔Y)BCO
a (Å)	3.8599	3.85118	3.85118	3.8599
b (Å)	3.9003	3.88642	3.88642	3.9003
c (Å)	11.67535	11.64215	11.64215	11.67535
$I(005)/I(004)$	17.5	23.9	31.3	10.4
$I(005)/I(007)$	5.85	2.96	2.87	5.9

ments for initial and one month old sample, but no further significant change later (figure 11). Also, a similar behaviour can be seen in Au-GdBCO. The steep initial reduction of $I(005)/I(007)$-ratio (from above 5.5 to below 3) would indicate a change of $\delta \approx 1$ which would mean that the sample has become non-superconducting within one month, but that is not seen in T_{c} measurements (figure 14, p. 34). Therefore, it is clear that the intensity ratios calculated for YBCO do not hold for GdBCO. That is why we have theoretically estimated the $I(005)/I(004)$ and $I(005)/I(007)$ intensity ratios for YBCO and GdBCO powders with FULLPROF x-ray diffraction pattern fitting program [112]. The used lattice parameters were good fits for respective powder patterns and they are presented in table 4. The simulations gave $I(005)/I(004) = 23.9$, and $I(005)/I(007) = 2.96$ for GdBCO, and for YBCO 17.5 and 5.85, respectively (table 4). To estimate further the effect of Gd on the ratios, we swapped the rare-earth cations (Gd ⇔ Y). The GdBCO lattice gave $I(005)/I(004) = 10.4$, and $I(005)/I(007) = 5.9$ with Y, and the YBCO lattice with Gd 31.3 and 2.87, respectively (table 4). The lower $I(005)/I(004)$-ratios of GdBCO lattice in comparison to the YBCO lattice may originate from the Gd–Ba-substitution [110, 111]. These results indicate that $I(005)/I(004)$ should be near 30, and $I(005)/I(007)$ above 2.9 for highly oxygenised and minimally cation substituted GdBCO. All the GdBCO films in this work seem to have a good oxygen content and some cation substitution. For BZO-doped samples the $I(005)/I(004)$-ratio is usually smaller for YBCO and higher for GdBCO and $I(005)/I(007)$-ratio is smaller for both in comparison to the undoped material. This indicates that BZO-doping has an effect on the ratios, since the results for BZO-doped material contradict each other, and nothing certain can be stated with the available data. The calculation of the real $I(005)/I(00l)$-ratios vs δ is not possible with the current data, since the determination of c parameter should be done for a spectrum of samples with different

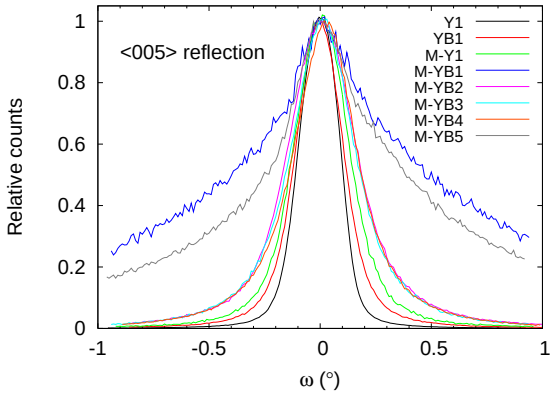

Figure 12. Broadening of the YBCO (005) rocking curve in different film structures. FWHM values of these curves are also listed in table 3 on the page 19. [**P3**]

oxygen content, which is necessarily needed because the peak intensities are result of interference, and therefore they are very sensitive to even minor variation of c.

Furthermore, the Au sputtering seems to have an effect on oxygen content as well, since the c-parameter is larger (figure 9), the $I(005)/I(004)$ higher, and $I(005)/I(007)$ lower for Au-coated samples in comparison to uncoated ones (figure 11), all indicating a reduced oxygen content in the Au-coated samples.

3.3.7 Line-widths

The full width at half maximum (FWHM) values are typically 0.32° for pristine YBCO and GdBCO (see for example table 2, p. 17 and figure 10) and slightly wider for the BZO-doped films, 0.36° or more. These are only slightly wider than the instrumental width, indicating a very small c-lattice parameter variation.

In YBCO/BZO multilayers, the YBCO (005) peak gets narrower as the thickness of the BZO layer decreases (table 3 p. 19). Also, the BZO (110) peak becomes broader as the BZO layer thickness reduces, and an extra broadening of BZO (110) peaks is observed when the BZO layers is few nanometres thick. This indicates a distortion in the cubic BZO lattice. Separation of size broadening from the strain broadening is not possible in practice.

Table 5. The rocking curve full width at half maximum values, initial critical current densities, J_c, and initial critical temperatures of uncoated-YBCO (uc-YBCO), gold-coated YBCO (Au-YBCO), uncoated GdBCO (uc-GdBCO) and gold-coated GdBCO (Au-GdBCO) thin films. [**P4**]

	uc-YBCO	Au-YBCO	uc-GdBCO	Au-GdBCO
Rocking curve (005) width (°)	0.25	0.25	0.20	0.20
Initial J_c at 10 K (MA/cm^2)	31.1	15.1	26.0	18.1
Initial J_c at 77 K (MA/cm^2)	2.16	0.85	3.15	1.83
Initial T_c (K)	89.0	89.0	91.5	91.5

3.3.8 Rocking curves

The out-of-plane structure has been studied by XRD rocking curves (ω-scan in figure 12). The FWHM of the (005)-peaks are usually 0.21°–0.26° (table 3, p. 19 and table 2, p. 17) for undoped YBCO and 0.19°–0.20° (table 5, p. 29) for undoped GdBCO. This indicates that GdBCO has a similar or better out-of-plane structure.

From the rocking curve values, a quantitative analysis can be made by calculating the coherence length [113]:

$$r_c = \frac{1}{\pi}\frac{d}{l\Delta\omega}, \tag{9}$$

where d is the lattice parameter c, l is the order of the Bragg reflection in question and $\Delta\omega$ is the FWHM of the rocking curve. All the single layered YBCO films (table 2, p. 17 and table 2, p. 17) have r_c higher than the threshold value of 10 nm for a good film [113]. Because in GdBCO, d and l are similar to all the YBCO and films and $\Delta\omega$ is lower, we can conclude that the r_c of GdBCO films (table 5) is above that threshold value, too, and therefore the quality of all the pristine films is good in this work.

The $\Delta\omega$ of YBCO (005) slightly increases and r_c decreases when YBCO is BZO doped (table 2, p. 17), but because the r_c is more than 10 nm, the ordering, and therefore the film quality, is high. The $\Delta\omega$ of multilayers with thick BZO layer is broad, which is usually connected to a strong mosaic spread [114]. Also, as stated above, the (005) peak broadens as the BZO layer becomes thicker. This agrees well with earlier results where the out-of-plane alignment enhances as the number of layers increases [45, 115]. The broadening of $\Delta\omega$ or the shortening of r_c is small with increasing thickness of the thin BZO layers, but with thick BZO layers, the $\Delta\omega$ widens and r_c shortens significantly,

which usually results in wider resistive transition widths and reduced J_c's [113, 116]. As it can be seen in table 3 on page 19 the decreasing trend of the r_c of YBCO correlate well with trend of r_c in BZO with reducing BZO layer thickness, therefore the thin BZO layers give a better c-axis alignment in comparison to the thicker and more distant ones.

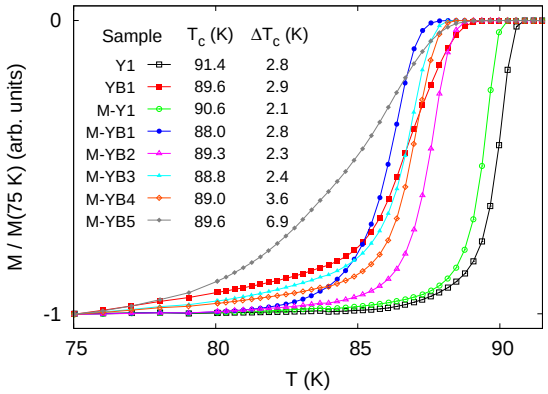

Figure 13. Normalised ac-magnetisation as a function of temperature for undoped and BZO-doped YBCO layers and YBCO/BZO multilayers. The inset table shows the onset critical temperature T_c and transition width $\Delta T_c = T_c^{90\%} - T_c^{10\%}$ values. [**P3**]

3.4 Superconducting properties

3.4.1 Optimisation of GdBCO thin film growth with PLD

All the undoped GdBCO films fabricated at T_s= 625–765°C had T_c higher than 90 K, and the J_c values were higher than 10 MA/cm^2 at 10 K and zero field, and higher than 1 MA/cm^2 at 10 K and 3 T. Hence, the deposition temperature is not as crucial for GdBCO as it is for YBCO, where below $T_\mathrm{s} = 700$°C the T_c decreases abruptly [87]. The optimisation of the GdBCO was done in order to achieve highest J_c at 10 K. The optimum temperature was 700°C, which is lower than for YBCO for which it is 745°C. The optimum energy density of the laser pulse depended on the target properties: the softer BZO-doped GdBCO target had a lower optimal energy density than the hard target of undoped GdBCO. This is reasonable, because the grains in a soft target are more easily detached than in a hard one.

3.4.2 Critical temperature, T_c

The T_c was determined from the onset value of the real part of the transition in the ac-magnetisation measurements at 0 T and as an onset in the resistivity measurements (figure 22 on page 45). The typical T_c of undoped YBCO determined by magnetization method is 88–91 K and is slightly higher, 90–92 K for undoped GdBCO. The literature indicates a higher T_c for GdBCO, too [73, 74]. The variation of T_c probably originates

from different oxygen contents of the films [62] or structural defects [110,111]. The typical T_c of 4wt% BZO doped YBCO and GdBCO is 90 K, and 87 K, respectively. It has been seen that the BZO-doping decreases the T_c in YBCO [49], which is in agreement with these results (see also figure 13). The transition width is definied as the temperature difference of 90% and 10 % values of the complete transition, $\Delta T_c = T_c^{90\%} - T_c^{10\%}$. ΔT_c is typically 1.7–2.8 K for undoped YBCO and 1.8–4.8 K for undoped GdBCO. As the T_c, the transition widths depend on the oxygen content and the structural defects [110, 111]. The BZO-doping also widens the transitions, the widths for 4 wt% BZO-doped YBCO and GdBCO are: 2.7–2.9 K and 4.1–7.1 K, respectively.

The resistivity measurements are in line with the inductive measurements, only the onset T_c's are slightly higher, 92.2 K for undoped YBCO, 93.0 K for undoped GdBCO, 92.2 K for 4 wt% BZO-doped YBCO, and 93.2 K for 4 wt% BZO-doped GdBCO. Similarly, the transition widths are narrower, 0.65 K, 1.3 K, 1.7 K, and 3.3 K for undoped YBCO and GdBCO, and BZO-doped YBCO and GdBCO, respectively. This can be explained by the current percolation, which means that the current finds the best path across the film which consists of the material with the best superconducting properties.

In the multilayers, the T_c reduces with the increasing BZO content, which can be related to the ratio of the YBCO and BZO layer thicknesses. This is also seen earlier: a decrease of T_c occurs in Y211/Y123 [117] and YBCO/CeO_2 multilayers [35], and a similar decrease with the increasing Y_2O_3 layer thickness [32,34], also in Ti, Zr, and Hf transition metals [41], and YSZ quasi-multilayers [118]. The transition width remains almost the same as the BZO layer thickness increases for thin BZO layers, but as the BZO-layers become thick, the transition widens dramatically for samples M-YB4 and M-YB5. The low temperature tail of the transition of the films with thick BZO-layers, particularly of M-YB5, indicates a reduction of the superconducting properties of a fraction of YBCO layers.

The explanation for T_c variation depends on the doping systems. For example, the transition metals form additions into the CuO planes [41], and the YSZ partially damages the YBCO due to the chemical reaction to form BZO [118], but adding Y_2O_3 reduces T_c because of the lattice mismatch, which might result in a charge transfer from the conducting CuO-planes to the Cu–O chains [34]. However, the BZO and YBCO phases are in balance in our multilayers, and no impurity phases were detected with XRD, therefore the most probable mechanism is the strain effect at the interfaces [44]. This also agrees well with the XRD results where different lattice parameters were found (table 3, p.19), which indicates strain. In case of M-YB5, the stress of YBCO

layers deposited on thick BZO layers can be estimated by using elasticity theory and approximating the tensile stress, σ [119]:

$$\sigma = E(\alpha_{\mathrm{YBCO}} - \alpha_{\mathrm{BZO}})\frac{\Delta T \Delta l}{d_{\mathrm{YBCO}}}, \tag{10}$$

where E is the Young's modulus of the layer at room temperature, α's are the thermal expansion coefficient of the layers, ΔT is the temperature variation, Δl is the lattice mismatch and d is the thickness of each layer. The following values are inserted to equation (10): $E = 210$ GPa for pure YBCO on STO [120], $\alpha_{\mathrm{YBCO}} \approx 13.4 \times 10^{-6}$ K^{-1} [121], $\alpha_{\mathrm{BZO}} \approx 7.13 \times 10^{-6}$ K^{-1} [122], $\Delta l \approx 0.35$ nm between YBCO and BZO, $d_{\mathrm{YBCO}} \approx 25$ nm, the change between deposition and room temperature, $\Delta T \approx 700$ K. These values estimated the stress, σ as 1.3 MPa. Such a high stress can distort the CuO-planes and widen the transition (figure 13) [44, 123]. For other multilayers, the situation is more complicated since the BZO layers are very thin. In their case the lattice mismatch and thermal expansion cannot be calculated from YBCO and BZO differences because the interfaces may not be continuous and well formed.

The change of the real part of ac-magnetisation with time is presented in figure 14 for undoped YBCO and GdBCO as well as for Au-coated YBCO and GdBCO. The decrease of T_{c} and widening of the transition can be seen in Au-coated GdBCO. They both originate from oxygen deficiency, which was shown in the sections 3.3.5 and 3.3.6. Its effect is clear, since the T_{c} decreases from initial 91.5 K to 66.5 K in five months. Also, the transition width widens from $\Delta T_{\mathrm{c}} = 3.3$ K to 14.6 K in five months. This is in accordance with [62], where it has been seen for YBCO that the transition broadens as the oxygen content decreases. Also the transition widths of Au-coated YBCO and GdBCO broadens in comparison to uncoated ones. This suggests that a phase with lower T_{c} has evolved on the top of the film. Therefore, sputtering seems to have an effect on the oxygen content as well, as it can be seen in the increased c-parameter lengths (see section 3.3.5 and figure 9), increased $I(005)/I(004)$-ratio and reduced $I(005)/I(007)$-ratio (see section 3.3.6 and figure 11, p. 26). According to the T_{c}-measurements, there seems to be no or very minor oxygen release in the uc-GdBCO and both YBCO samples (figure 14).

3.4.3 Critical current density, J_c

All the critical current densities, J_{c}'s, were calculated from inductive data with Bean model described in the section 2.2.2. The J_{c}'s of the YBCO films, F1–F4, ablated from targets with different densities, are shown at 10 K and 70 K in figure 15 and the J_{c} values

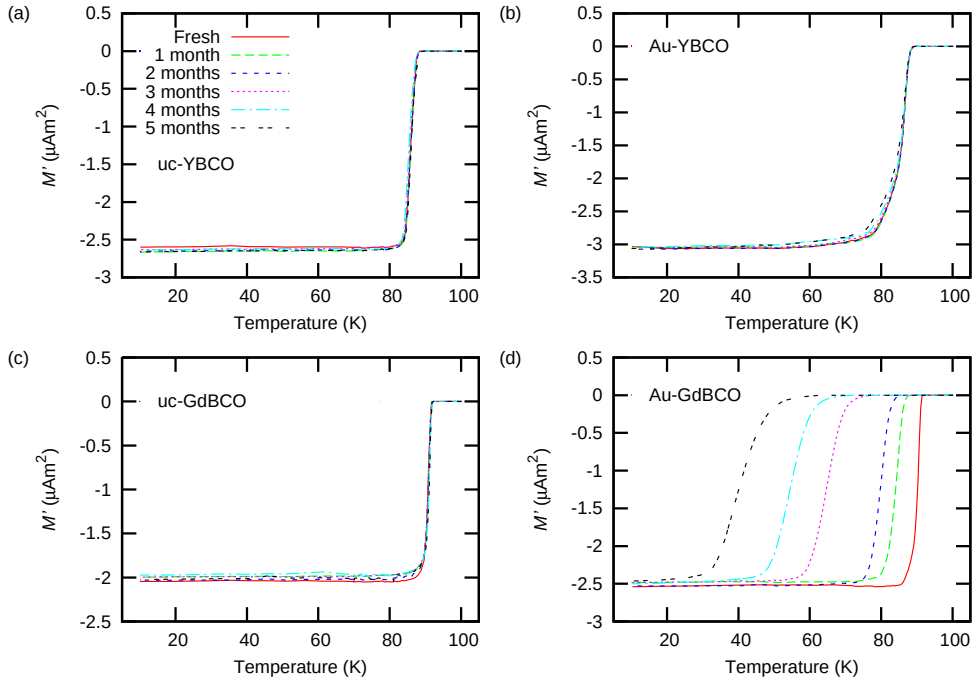

Figure 14. The real part of ac-magnetisation M' and its time dependence in uc-YBCO (a), Au-YBCO (b), uc-GdBCO (c) and Au-GdBCO (d). [**P4**]

at 10 K and zero field are presented in table 2 on page 17. The J_c has a similar behaviour in the whole measured temperature region, 10–80 K. It can be seen that the scattering of the J_c's at low fields disappears completely at high fields, and all the films have the same dependence at high magnetic fields. This means that the nature and distribution of the pinning sites are probably the same in all the films.

There is also no change in the form of the J_c curves, which is the low field plateau and curve shape at high fields, for all the undoped and uncoated or Au-coated YBCO and GdBCO with time (figure 16). Hence, this confirms that the pinning structure has not changed, which is in accordance to the XRD measurements of (212)/(122)-peak that did not show any major changes with time. Therefore, the reduction of J_c with time in uc-YBCO, uc-GdBCO, and Au-GdBCO (figure 16(b), (c), and (d)), is also due to the oxygen release as it has been discussed in previous sections. A reduction of J_c is seen in uc-GdBCO for the first two initial months, but the decrease saturates in the subsequent months (figure 16 (c)). There is some minor variation of J_c in the last three months, which is similar to YBCO, where some variation can be also seen (figure 16

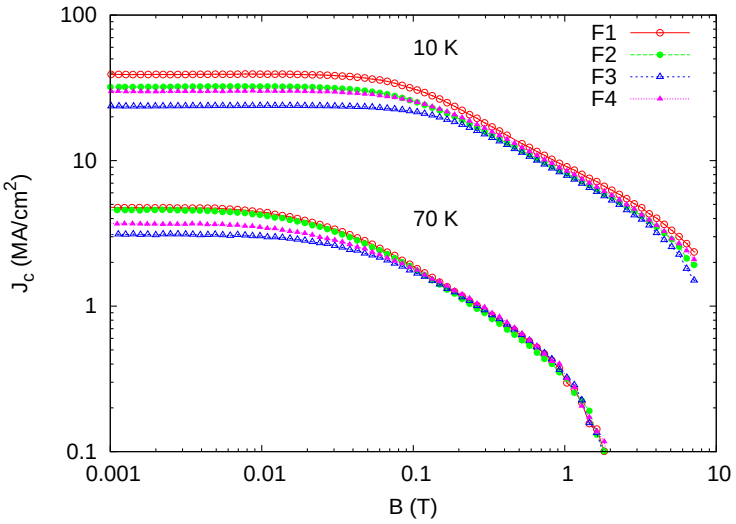

Figure 15. The magnetic field dependence of J_c for samples F1–F4 at 10 K and 70 K. [**P2**]

(a)); however, the abrupt decrease of the J_c between measurements done for the two and three months old sample, is probably due to a split or scratch that appeared on the surface of the film on that time. The small variation might originate from some interaction with air. In Au-GdBCO the reduction is fast: from 18.1 MA/cm^2 to 1.01 MA/cm^2 in five months (figure 16 (d)). The sputtering also has an effect on the J_c in both materials (figure 16 and table 5), p. 29).

In paper [**P1**] the J_c(10 K, 0 T) of the undoped GdBCO is higher than in YBCO which was ablated for the same work to compare the results of GdBCO with YBCO. As it can be seen in figure 17 (a), undoped GdBCO has a better J_c than YBCO below 1 T and at 10 K, similarly at higher temperatures (see figure 17 (b)). The J_c(10K, 0T) of undoped YBCO agree well within paper [**P1**] and [**P4**] but the value is lower in paper [**P4**] than in paper [**P1**] for undoped GdBCO (table 6). To ease the J_c comparison in paper [**P1**], the J_c(77 K, 0 T) was estimated with an equation

$$J_c \propto \exp(-T/T_0), \tag{11}$$

where T_0 is the fitting parameter, and it estimated 2 MA/cm^2 for both the undoped material (table 6). In paper [**P4**], the J_c(77 K, 0 T) for YBCO was similar to the value in [**P1**], but higher for GdBCO (table 6). So, the J_c's of YBCO agree well between these two papers, but there is a small discrepancy in case of undoped GdBCO. This

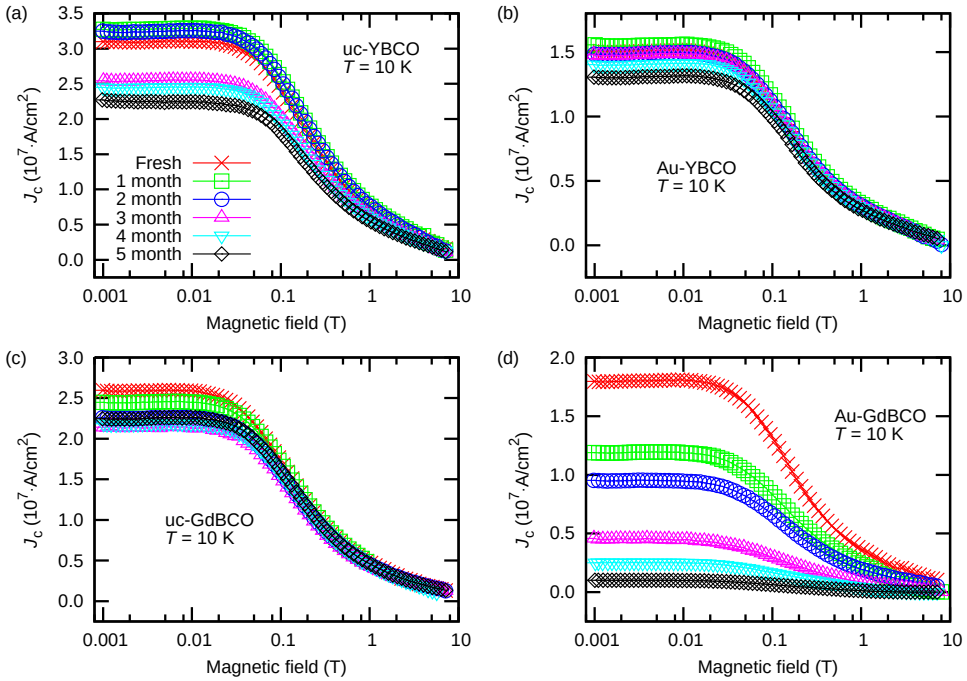

Figure 16. The J_c measurements of the fresh and the aged uc-YBCO (a), Au-YBCO (b), uc-GdBCO (c) and Au-GdBCO (d) thin films. [**P4**]

Table 6. The J_c(0 T) values at 10 K and 77 K for various YBCO and GdBCO films.

	YBCO	GdBCO	Paper
J_c(10 K, 0 T) (MA/cm^2)	31.1	26.0	[**P4**]
J_c(77 K, 0 T) (MA/cm^2)	2.16	3.15	[**P4**]
T_c (K)	89.0	91.5	[**P4**]
J_c(10 K, 0 T) (MA/cm^2)	30	33	[**P1**]
J_c(77 K, 0 T) (MA/cm^2)	≈ 2	≈ 2	[**P1**]
T_c (K)	90	91	[**P1**]
	YBCO+4wt% BZO	GdBCO+4wt% BZO	
J_c(10 K, 0 T) (MA/cm^2)	13	49	[**P1**]
J_c(77 K, 0 T) (MA/cm^2)	≈ 2	≈ 0.2	[**P1**]
T_c (K)	90	87	[**P1**]

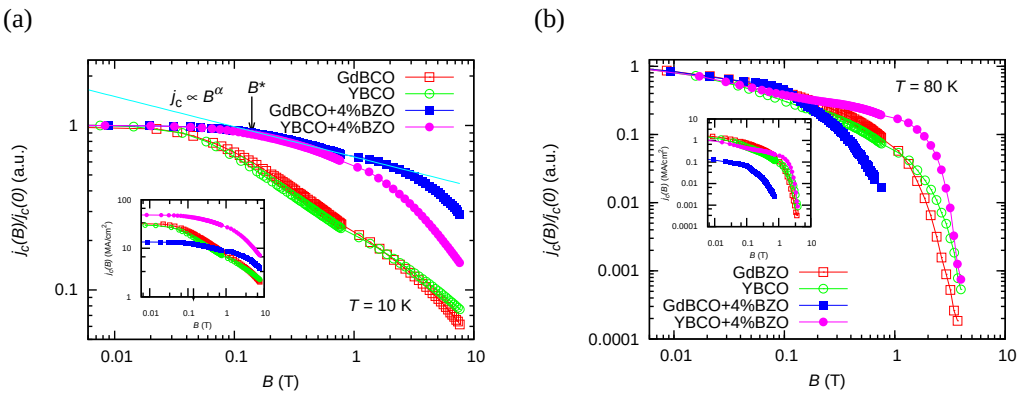

Figure 17. Field dependence of normalised J_c at 10 K (a) and 80 K (b) for optimised undoped and doped GdBCO and YBCO films; for undoped ones: hollow boxes and bullets, respectively and for doped ones: filled boxes and bullets, respectively. The insets show the absolute $J_c(B)$ values. [**P1**]

contradiction might originate from high T_c of the GdBCO film made for paper [**P4**] (table 6): it was ≈ 92 K whereas the T_c of undoped GdBCO was ≈ 91 K. This suggests that undoped GdBCO grown for paper [**P1**] contains more defects or stronger pinning sites giving higher J_c at low temperature, but these defects reduce the T_c and therefore the J_c is decreased at high temperatures [124].

The best BZO-doped GdBCO film had J_c(10 K, 0 T) $= 13$ MA/cm^2. This value was lower than the extraordinary high J_c(10 K, 0 T) $= 49$ MA/cm^2 in BZO-doped YBCO fabricated for comparison (figure 17 (a) and table 6). Since the pinning properties are similar at high magnetic fields but there is some variation in J_c(0 T) for the set of films made from the targets of different densities (see the text above and figure 15), it is concluded that the J_c(0 T) depends on the quality of the superconducting properties (such as carrier density etc.) of the material, not the pinning properties. Therefore, the normalised J_c's are used to ease the comparison of the pinning properties in figure 17. The interpolation with equation (11) at 77 K estimated 0.2 MA/cm^2 and 2 MA/cm^2 for BZO-doped GdBCO and YBCO, respectively (table 6). The latter agrees well with recent value found in literature for BZO-doped YBCO [43]. The low J_c of BZO-doped GdBCO is result of the low T_c (table 6). The BZO doping enhances the J_c field dependence at high fields and low temperatures, and hence this strengthens the hypothesis that BZO grows as nanorods in GdBCO as in YBCO. Furthermore, the 4 wt% BZO-doping is more effective in GdBCO than in YBCO (figure 17) at fields higher than 0.8

T. At high temperatures the BZO-doping does not improve the pinning, and it may even worsen the properties of the GdBCO by lowering the T_c. This result is in agreement with recent results, where 4 wt% BZO-doping was observed to be most effective in YBCO at low temperatures [49, 51].

The fact that BZO-doping is effective at low temperatures, also holds with BZO multilayering, as it can be seen in figure 18. To ease the discerning of the differences between the films, the black contour lines represent constant J_c values of 10, 5, 2, and 0.5×10^{10} A/cm^2. The YB1 and M-YB4 have the best J_c values in the whole temperature range. However, the undoped YBCO is the best material at high temperatures and in the low magnetic field range. The thick BZO-layers, M-YB1 and M-YB5, suppress the superconducting properties and pinning force, which is seen as a reduction of the J_c at all the measured fields and temperatures (figure 18) [44]. This is in accordance with the structural measurements (section 3.2 and table 3, p. 19) where smoother surface produces higher J_c, and therefore it can be concluded that the surface pinning does not play an important role in pinning of multilayers [125, 126]. Further, the results show that the variation in the c-parameter lowers the J_c especially in the samples of thick BZO-layers, M-YB1 and M-YB5, and thus the stress formed between the layers does not induce defects that are strong pinning sites. Also, a correlation between J_c and lattice coherence, r_c, is found, and therefore the thickness of a single layer is important if thicker multilayer films are desired. Thus, a optimisation of the multilayer structure must be done for finding an optimal pinning structure simultaneously at the temperature and magnetic field needed for the particular application.

In order to compare the shapes of the $J_c(B)$ curves at different temperatures, a double logarithmic line fitting was made with power law equation (4) on page 3. The lower limit of the fit is the accommodation field which is defined from equation (3) on page 3, see section 1.1.2 for more details. The upper limit is the crossover of strong pinning and flux creep, which is seen as a change of the slope in the linear fit in the double logarithmic plot (figures 17(a) and 21(a)). The change in the data spacing and the small step in $J_c(B)$ at 1 T in figure 17 is due to the change in the magnetic field scanning rate, and it has no effect on the fitted α values.

The $B^*(T)$-curves have a negative curvature (figures 19, 20(a), and 21(a)), which is also seen in literature, ref. [127]. Also, the B^*'s can be described with an exponential law:

$$B^*(T) = B_0^* e^{(-T/T_0)}, \tag{12}$$

where the characteristic temperature T_0 describes the decrease rate of B^* with increas-

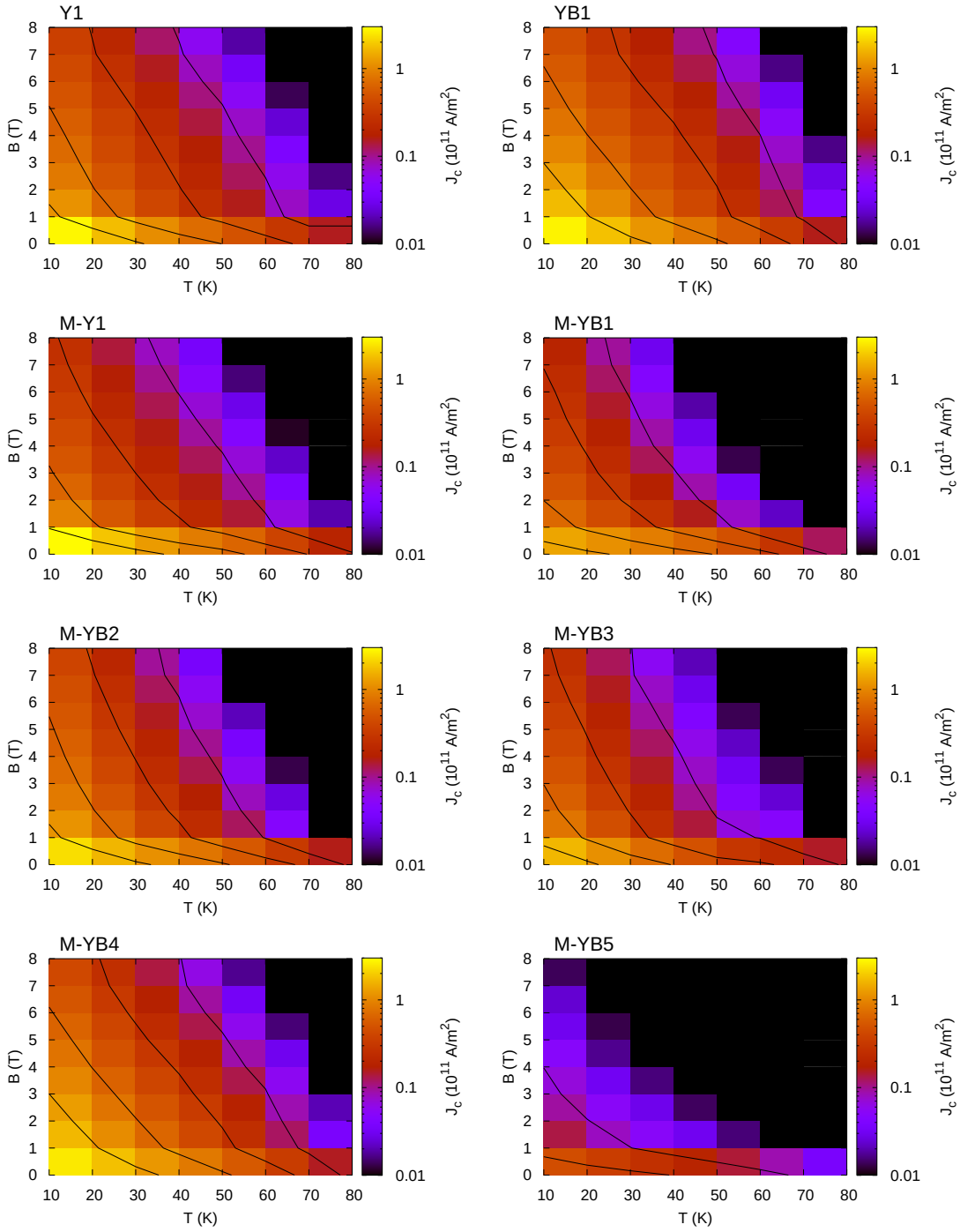

Figure 18. Temperature and magnetic dependences of j_c for different multilayer structures in logarithmic colour scale. The lines of constant j_c (from left to right of 1, 0.5, 0.2 and 0.05 $\times 10^{11}$ A/m^2) are shown as black contour lines. For M-YB5 only two lowest values 0.2 and 0.05 $\times 10^{11}$ A/m^2 are visible. [**P3**]

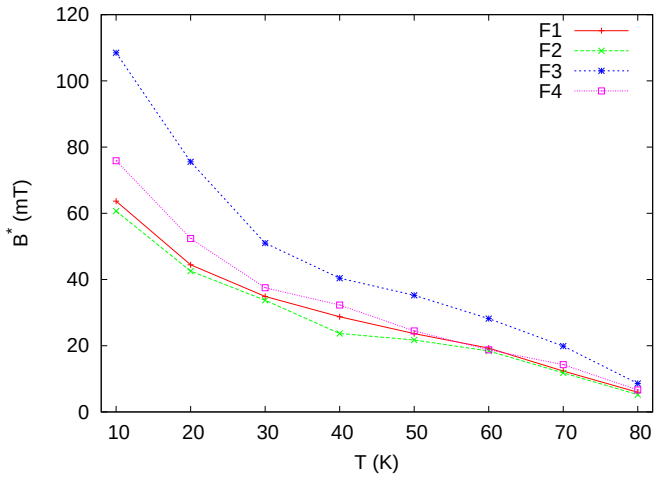

Figure 19. The temperature dependence of the accommodation field B^* for films F1–F4. [**P2**]

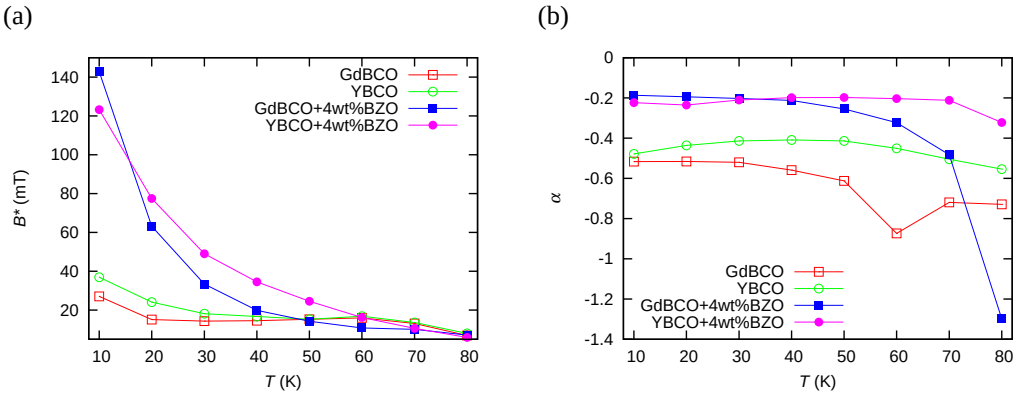

Figure 20. Temperature dependence of B^* (a), temperature dependence of the exponent α (b) for undoped and BZO-doped YBCO and GdBCO films in [**P1**].

ing temperature [127, 128]. The fit parameters B_0^* and T_0 are listed in table 7 for multilayered films. It should be noted that the direct comparison of the B^*'s in table 2 on page 17 and table 7 and figures 19, and 20(a) should not be done, because firstly, the magnetic field scanning rate and data point spacing are not the same for figure 20(a) as for rest of the presented data, and secondly, because the data in table 7 are extrapolated to 0 K. However, the B^* values of all the measurements can be related by values of undoped, single layer YBCO thin films of each measurement, since they should have

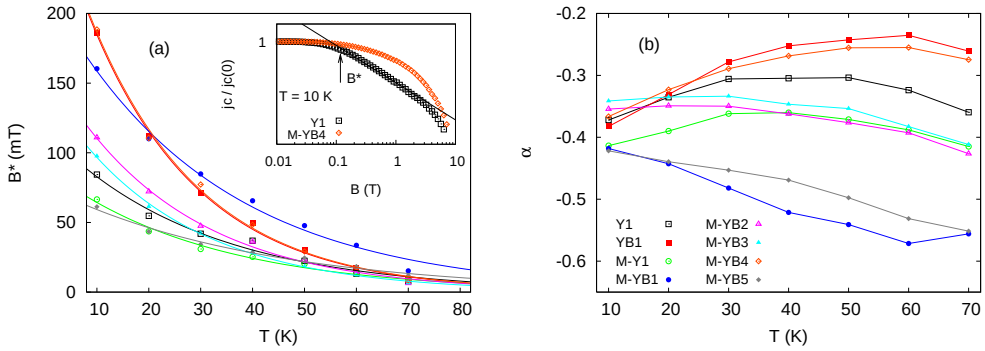

Figure 21. Temperature dependence of the accommodation field B^* for different multilayer structures (a), where the lines are fits to equation (12). (b) Temperature dependence of the exponent α, when the field dependence of J_c is fitted to the equation (4) on page 3. [**P3**]

Table 7. Values of accommodation field at 0 K B_0^* and characteristic temperature T_0 calculated from the fits to equation (12) for different multilayer structures. [**P3**]

Sample	Y1	YB1	M-Y1	M-YB1	M-YB2	M-YB3	M-YB4	M-YB5
B_0^*(mT)	117	296	89	222	167	147	298	77
T_0(K)	29	21	30	30	24	23	21	38

almost the same properties even though the different methods result in slightly different values.

By comparing the B^* and other values in table 2 on page 17, it can be seen that B^* correlates negatively to J_c(0 T), but positively to the structural values which represents lattice faults (FWHM of (005), $\Delta\omega$, r_c, $I(005)/I(004)$, and even thickness), but there is no correlation to the T_c and the target density. This confirms that the enhancement of superconducting properties of the films made from nanograined targets in comparison micronsized targets [25, 51] is due to the smaller grainsize. Therefore, the lattice defects formed during the PLD ablation widen the XRD peaks and increase the number of pinning sites which is seen as higher B^* values. The increased number of defects reduce J_c [11]. However, it is worth noting that the films F1–F4 have similar J_c field dependence, and thus the small variation of J_c(0 T) does not affect the applicability of the films. In addition, if one wants to enhance the field properties at high fields, one should change the pinning structure radically, e.g. by adding BZO nanorods, some other perovskites or apply multilayering.

The BZO-doping and multilayering indeed enhance the low field properties of the REBCO films, as it can be seen in figure 20(a) and 21(a) and table 7, where BZO nanorods improve the B^* (and B_0^*) of YBCO and GdBCO, as well as thin alternating BZO and YBCO multilayers, M-YB4. In addition, B_0^* is smaller in samples which do not contain BZO-doping and in those where the BZO layers are extremely thick. Also, the B_0^* of Y1 is higher than of M-Y1, where a relaxation occurs in each layer. The results above agree with results where the increased B^* is associated with the high density of correlated defects [11,17,129]. The higher T_0 values indicate gentler temperature dependence of the pinning properties, which occurs in the thick YBCO layers without disturbing dopant layers. The B^* values in figure 20(a) are lower than the others presented in this work, since the scanning rate and data spacing were higher at low fields in magnetisation measurements, which results in underestimation of B^*. In GdBCO, the B^* is similar to the value in YBCO. The BZO-doping enhances the B^* as it does in YBCO, thus it confirms that BZO grows as nanorods in our GdBCO as it is seen for YBCO grown from nanograined targets [25]. Furthermore, because the increase of B^* in BZO-doped GdBCO is steeper than in the respective YBCO film at low temperatures, and because as stated above, the J_c enhancement is more effective at 10 K (figure 17), the BZO-doping is more effective in GdBCO than in YBCO.

The power law (4) exponents, α's, are presented in figures 20 and 21. The α-values of the films F1–F4 are ≈ -0.5. Their similar values indicate that the target density has no effect on the pinning structure, which was expected. Also, the value of -0.5 is typical to the undoped YBCO films [49] where the pinning structure consists of twin plains and dislocations [8]. Furthermore, although the $\alpha(T)$ is usually temperature independent, but the films with high number of dislocations have a decreasing curvature with increasing temperature [9–11]. According to the figure 21(b) the multilayers can be categorised into three different groups of slightly different pinning mechanisms. The structure of the thin BZO and YBCO layers, the M-YB4 film, is the only one which induces similar pinning structure to c-axis correlated BZO-nanorods in YB1. In literature, it has been shown that the BZO nanorods have double volume in comparison to the density of the BZO grains, which means that the half of a nanorod volume consists of distorted YBCO, but the BZO particles still align in c-direction [59]. Therefore, the similar α-values with BZO-doped YBCO indicates that the dense BZO network is not only aligned horizontally but as well in c-direction of YBCO. A similar α values, -0.2–-0.3, is also found in BZO-doped YBCO and GdBCO in figure 20. These values agree with those found in literature [33,48,49]. This strengthens the hypothesis that

BZO grows as nanorods in GdBCO. In the multilayered films with relatively thick BZO-layers, M-YB1 and M-YB5, the α has a decreasing trend with increasing temperature whereas the α is temperature independent for rest of the films.

All these results show that there are several crossovers of pinning in c-axis direction, and it varies from strong individual pinning to weak collective pinning with temperature and magnetic field strength. Therefore, if the highest possible J_c is needed at low temperatures and high magnetic fields, the BZO-doping should be applied to YBCO or GdBCO, the latter being slightly more tempting, or multilayering with thin alternating BZO and YBCO layers, which is the only multilayer structure comparable to BZO-doping. On the other hand, as it seems that the thin alternating BZO/YBCO multilayers produce smoother film surface, and this structure may allow a higher overall thickness of the films without decrease of critical current density, allowing higher critical currents for thick films. However, the GdBCO is also favourable for the thick film growth, and it might be more desirable because of the simpler growth procedure.

3.5 Resistivity of undoped and BZO-doped YBCO and GdBCO

3.5.1 Resistivity measurements in the temperature activated flux-flow (TAFF) regime

The resistive transition curves, $\rho(T)$, in both $B \parallel c$- and $B \perp c$-direction are presented in figure 22. The normal state resistivities are similar to those found in literature for the undoped GdBCO [130] and YBCO thin films on STO [131]. The transition were narrower in $B \perp c$ than $B \parallel c$ geometry because of the intrinsic pinning of the CuO planes. In addition, the transition is narrower for the undoped samples in comparison to the doped ones.

All the measured data in the TAFF regime could be described with (6) (derived on page 4). The obtained U_0's are presented in figure 23. The higher U_0 indicates a higher pinning, and it is higher for undoped YBCO than for undoped GdBCO in both the directions, $B \parallel c$ and $B \perp c$. The BZO-doping decreases U_0 in both materials in the whole magnetic field range in $B \perp c$ direction. The both mentioned lowering of the pinning potential can be attributed to distorted ab-planes. In the $B \parallel c$ direction, the 4 wt% BZO-doping increases U_0 in 1–8 T magnetic field range in YBCO, and the similar doping has an increase of U_0 only above 3 T in GdBCO (figure 23(a)). On the other hand, from the tendency of the curves one can estimate that the BZO-doped GdBCO has the highest U_0 above 8 T. However, the U_0 is lower for BZO-doped GdBCO than for the rest of the films in the low field region. Therefore, BZO seems to destroy some strong pinning sites or lower their pinning potential; these pinning sites may be such as twin boundaries [5] and dislocations [132].

The irreversibility field, B_{irr}, is the field below which the vortices are trapped to pinning sites so that the thermal fluctuations are not able to depin them. In this work, the B_{irr} is defined from 10^{-3} value of the normal resistivity just above the transition, $\rho_{\mathrm{N}} = \rho(94\ \mathrm{K},\ \mathrm{self\ field})$, and it is shown in figure 24. The B_{irr} of undoped GdBCO does not exceed the values of YBCO in either of the directions. Also in the $B \perp c$ direction, the decrease of B_{irr} is gentler at high temperatures in undoped and BZO-doped GdBCO than in low temperatures, which is not seen in the YBCO films. These phenomena can be related to the more distorted ab-planes in GdBCO than in YBCO, which is discussed in more detail in the section 3.5.3. The decrease of B_{irr} in the BZO-doped samples can be related to the decrease of T_{c} by 'poisoning' of the superconducting properties with the BZO-doping [49, 133, 134]. In $B \parallel c$, at 3 T and below, the B_{irr} is higher for undoped GdBCO in comparison to doped GdBCO at high temperatures (figure 24(a)). On the

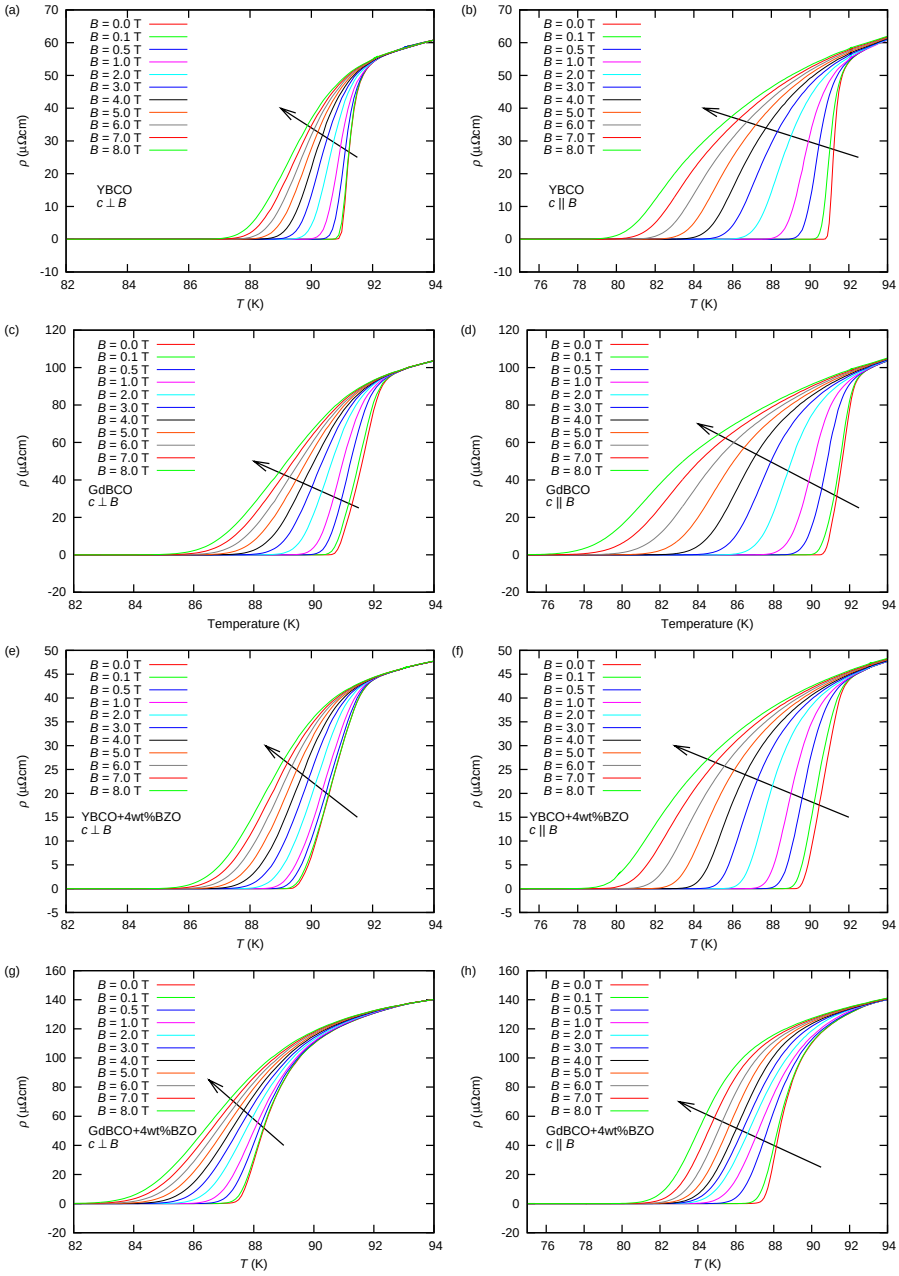

Figure 22. The resistivity curves for YBCO (a) and (b), GdBCO (c) and (d), YBCO+4wt%BZO (e) and (f), as well as GdBCO+4wt%BZO (g) and (h). The external magnetic field B was perpendicular to the c-axis on the left hand side and along the c-axis on the right hand side. The arrows indicate the increasing external magnetic field. [**P5**]

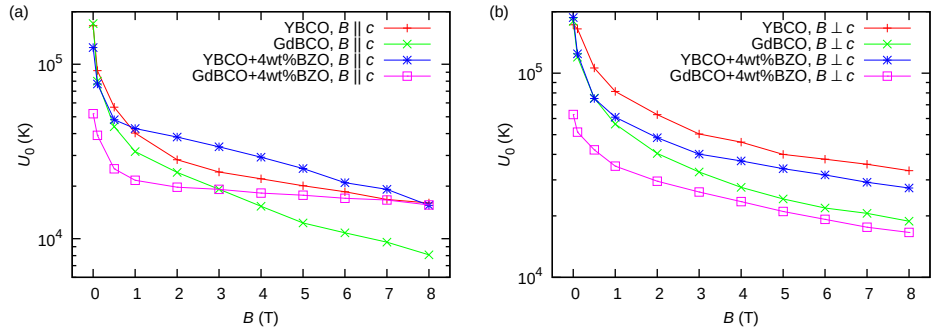

Figure 23. The pinning potential, U_0, as a function of applied field along the c-axis (a) and perpendicular to the c-axis (b). [**P5**]

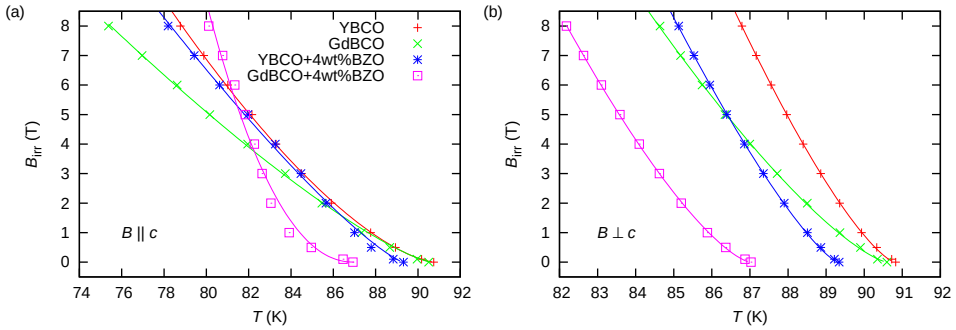

Figure 24. The irreversibility field, $B_{\rm irr}$, as a function of temperature in $B \parallel c$ (a), and in $B \perp c$ (b). The lines are fits to the power law of $B_{\rm irr}$ given in the text. [**P5**]

other hand, the BZO-doping becomes effective above 3 T. In addition, the BZO-doping seems to be more effective on $B_{\rm irr}$ in GdBCO, since at high temperatures BZO-doped GdBCO has the lowest $B_{\rm irr}$, but below 81.5 K it is opposite. The $B_{\rm irr}$ of BZO-doped YBCO does not exceed the $B_{\rm irr}$ of undoped YBCO at any point, and the reason for this is the superconducting properties (narrow transition, high $B_{\rm irr}$, and U_0), which are better than in an earlier measured undoped YBCO sample in our group [16]. A power law [7, 135]:

$$B_{\rm irr} \propto [1 - (T/T_{\rm c0})]^{\beta}, \tag{13}$$

where β is the free parameter and $T_{\rm c0}$ is taken as the temperature, where $B_{\rm irr} =$ self field, because at $T_{\rm c}$ the $B_{\rm irr}$ is zero, could be fitted to all the data [5]. The fitting parameters are listed in table 8. The vortex lattice melting theory predicts $\beta = 2$, but usually it

Table 8. The fitting parameters for power law, $B_{\rm irr} \propto [1-(T/T_{\rm c0})]^{\beta}$, fits.[**P5**]

Sample	$T_{\rm c0}$(self field) (K)	$\beta(B \parallel c)$	$\beta(B \perp c)$
YBCO	90.8	1.50	1.35
GdBCO	90.6	1.27	1.34
YBCO+4wt%BZO	89.3	1.23	1.38
GdBCO+4wt%BZO	87.0	2.18	1.39

varies between 1.35 and 1.45 [5]. The β in our undoped GdBCO in the $B \parallel c$ direction is smaller than 1.28 that is reported in reference [7], but the $B_{\rm irr}$(77 K) = 7 T of our sample is higher than $B_{\rm irr}$ = 4 T of their sample; however, they probably have a different criterion for $B_{\rm irr}$, therefore the $B_{\rm irr}$ values cannot be directly compared. In the $B \perp c$ direction, β of YBCO is higher than β of GdBCO. The latter is the same as in [7], and the $B_{\rm irr}$ we determined is again higher than theirs. Because low β indicates higher isotropy, which results in higher $B_{\rm irr}$ [136], low β is desired [137]. Hence, GdBCO is more isotropic than YBCO. The β is decreased in YBCO but increased in GdBCO by BZO-doping. At first, this would be in contradiction with the above, since undoped YBCO and particularly the BZO-doped GdBCO have $B_{\rm irr} = 8$ T at the highest temperature in $B \parallel c$, but they both have the highest β's in $B \parallel c$-direction. However, the contradiction may have arisen from the different upper critical fields, $B_{\rm c2}$'s, the samples may have, since $B_{\rm irr}$ is proportional to $B_{\rm c2}$ [5]. Furthermore, the too high β of BZO-doped GdBCO may be also due to equation (22) not describing the high temperature data perfectly. In the $B \perp c$ direction, the β values of undoped GdBCO and YBCO are close to each other. The β's are almost the same between the doped samples, too, but their β's are slightly higher than β's of undoped YBCO and GdBCO.

3.5.2 Resistivity vs. magnetic field rotation angle, $\rho(\Theta)$

The normalised resistivity as a function of magnetic field angle, $\rho(\Theta)/\rho_{\rm N}$, where $\rho_{\rm N} = \rho(94\ {\rm K},\ {\rm self\ field})$, for undoped YBCO and GdBCO as well as BZO-doped YBCO and GdBCO are shown in figure 25. The curves were chosen so that the normalised resistivities are close to each other in undoped GdBCO and YBCO as well as in the BZO-doped ones. Since the resistivity of the samples depend on temperature, the measurement temperatures are also indicated. The c-axis peak (at 90°) is clearly wider for undoped GdBCO than for YBCO (figure 25(a)), further, the $\rho(\Theta)$ is more isotropic.

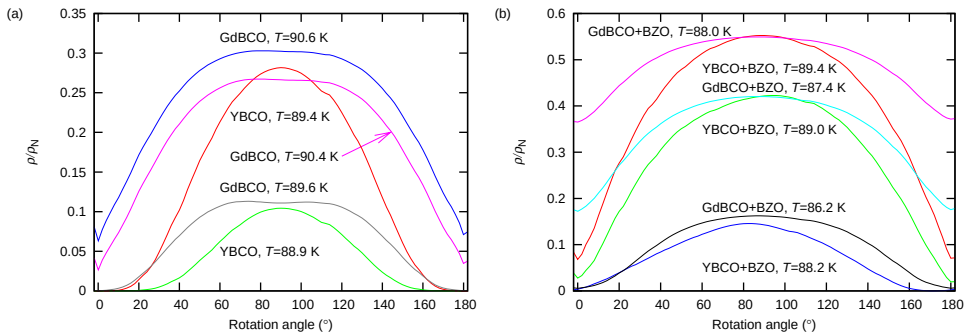

Figure 25. The resistivity versus magnetic field angle of undoped YBCO and GdBCO (a) and BZO-doped YBCO and GdBCO (b), where 0° corresponds to $B \perp c$ or to $B \parallel ab$-plane and 90° $B \parallel c$. The applied magnetic flux density was 1 T. Since the resistivity depends on the temperature, the curves were chosen so that the normalised resistivity would be close to each other in undoped YBCO and GdBCO, similarly in the case of the doped samples. The measurement temperature of the individual curves are shown. [**P5**]

That and a dip at 90° in undoped GdBCO, are perhaps a result of the resistivity exceeding the threshold value, which is seen in some YBCO samples [131]. The BZO-doping widens the c-axis peak, and increases isotropy (figure 25(b)). These results except for the BZO-doped GdBCO sample agree with the β values discussed in the previous section. Furthermore, there is an agreement with the previous J_c measurements at 1 T and 77 K [52–55], which show that the undoped GdBCO is more isotropic than YBCO and that BZO-doping increases isotropy, although the huge c-axis peak observed in J_c measurements [8, 12, 52–55] is not seen in our $\rho(\Theta)$ measurements. It is due to temperatures higher than irreversibility temperature, T_{irr}, where the vortex lattice melts [138]. The increased isotropy in GdBCO compared to YBCO has been attributed to the extra stacking faults in GdBCO [52], and increased isotropy in the BZO-doped materials has been related to the c-axis correlated defects [52, 53, 55].

3.5.3 Discussion

As already mentioned, the higher pinning potential, U_0, and irreversibility field, B_{irr}, in undoped YBCO compared to undoped GdBCO and further, undoped materials in comparison to doped ones, are explained by more intact ab-planes. In the former case, the ab-planes of GdBCO are distorted probably due to the extra stacking faults which result

in edge dislocations or wavy ab-planes [21,55,74]. In the latter case, the BZO nanorods create dislocations in their vicinity [25], which probably results in wavy ab-planes, too. The wavy ab-planes have a lower pinning, because the ab-planes have the pinning at strongest when the magnetic field is exactly parallel to them, and therefore some parts of the wavy ab-planes are not at such an optimum position. In non-parallel ab-plane the vortex tends to align to the magnetic field or whatever is the lower energy path and become staircase-like [139, 140], which result in a wider J_c-peak at $B \parallel ab$-plane. This is difficult to determine unambiguously from the J_c-data available which show a wider J_c-peak for GdBCO at 1 T and below [55,74], because the random pinning sites play a role, too [139]. However, the data are in good agreement with the discussed B_{irr}-data above, because there is a wider J_c peak for GdBCO than for YBCO at 1 T and 77 K but at 3 T the widths seem to be very similar [74]. Hence the observed U_0 and B_{irr} result from the wavy ab-planes, and it is worth noting that probably the more isotropic behaviour of undoped GdBCO and BZO-doped material in comparison to undoped YBCO does not only result from the improvement of J_c in the c-axis direction but also from the reduction of intrinsic ab-plane pinning.

The results above indicate that the same 4 wt% BZO doping has more effect on GdBCO than on YBCO: at low fields, U_0, B_{irr}, and J_c decrease more, but at high fields U_0 and B_{irr} increase more, J_c increases more at low temperatures in the $B \parallel c$ direction, and in $B \perp c$ direction U_0 and B_{irr} are reduced in the whole measured magnetic field range. This can be partly explained by the 10 % higher weight of GdBCO in comparison to YBCO, where the volume of the unit cell is only 1 % larger for GdBCO than for YBCO, so hence the volume of the BZO would be higher in GdBCO. However, this does not explain the whole difference. Since the lattice mismatch between GdBCO and BZO (7.9 %) is lower than betwenn YBCO and BZO (8.4 %), it can not explain the difference either. Thus, three different explanations have been considered:

1. The first one might be the easier cation disorder in GdBCO than in YBCO, since the size of the Gd^{3+} ion is closer to the size of Ba^{2+} than of Y^{3+}. If significantly Ba poor regions, which would have significantly lower T_c and J_c [97], are formed, they could behave as pinning sites, which might be the case in SmBCO [137].

2. The second possible explanation would be the stress caused by BZO-doping with interplay of extra stacking faults. As was discussed in section 3.3.3 on page 21, the (212)/(122)-peak shows reduced relaxation by twinning and more stress in BZO-doped GdBCO. The origin of this extra stress may be the extra stacking faults present in GdBCO [21]. Such a stacking fault can be an extra Gd-layer,

which is formed due to the easier occurrence of the Gd⇔Ba cation disorder. The layer causes a shift of $[(1/2)a, (1/2)b, 0.15c]$ [21] which produces stress, if it is energetically favourable BaO layers to match between GdBCO and BZO. The shift would have an influence on a and b parameters, which would agree with the results in section 3.3.3. Further, the increased stress might also affect the T_{c} and which has been observed earlier for YBCO in [141, 142] and references therein. Furthermore, the shift or the strain might also produce splay on the BZO nanorods, which could improve the J_{c} [143–145].

3. The final considered possibility is the oxygen deficiency, which is known to reduce T_{c} [61, 62]. The $I(005)/I(00l)$ analysis in the section 3.3.6 on page 25 does not undoubtedly strengthen this possibility, but does not rule it out either, at least it is possible in some parts of the material.

Thus, all these tree explanations assumes a generation of nanoscaled regions with reduced superconducting properties which behave as pinning sites. The nanoscaled phases with reduced T_{c} and superconducting properties would explain the change of the slope of B_{irr}-curve of BZO-doped GdBCO (figure 24(a)), since a change in T_{c} of a nanosized region would result in a contribution on B_{irr} merged from all the nanophases with different B_{irr}'s, and that is why equation (13) does not describe the observed B_{irr} perfectly. Also, the reduction of T_{c} would not only influence the pinning directly, but also indirectly by changing the coherence length, ξ, near the T_{c} [5], which has an effect on pinning strength, since the optimum pinning site should have a size of ξ.

3.6 X-ray photoelectron spectroscopy

The X-ray photoelectron spectroscopy (XPS) measurements were done to study the oxidation state of Cu in fresh and seven months old, undoped and uncoated GdBCO thin films. The initial measurement was made a day after the film deposition, and the final measurement for the aged sample seven months later. To measure the bulk Cu atoms without surface contamination, the surface of both films were sputtered with Ar^+ ions with the same parameters for the both times until the C $1s$ impurity signal was almost completely vanished. The core-level spectra Cu $2p_{3/2}$ and O $1s$ of the fresh (○) and aged (●) GdBCO are shown in figure 26. A fitting was done with Voigt line-shape and Shirley background subtraction was applied to identify and confirm the different components and their relative intensities. The peak positions agree well with reported data [146–149], and the observed Cu $2p_{3/2}$ main line and the Cu satellite feature show the known structure of CuO and Cu_2O [146, 150]. The Cu $2p_{3/2}$ spectrum consists of the CuO and Cu_2O photoemission lines with 1.2 eV binding energy (BE) separation, where CuO is on the high BE side. The satellite structure above the Cu $2p_{3/2}$ BE is characteristic to CuO, and no such a satellite can be seen for samples containing only Cu_2O [150, 151]. A weakening of the CuO satellite with time suggest strongly that the amount of CuO has reduced. Indeed, the intensity ratio ($I_{\mathrm{CuO}}/I_{\mathrm{Cu_2O}}$) which was calculated from the areas of CuO satellite and Cu $2p_{3/2}$ signal of Cu_2O for the fresh and aged sample decreased from about 0.5 to 0.2. Also, two features can be clearly resolved from the O $1s$ spectra of both the measurements (figure 26 inset). The feature at 529 eV is due to the Cu-O chains and planes, and the component at 531 eV higher BE side is caused by oxygen contamination [146, 148, 152]. Moreover, despite of the removal of the carbon contaminated surface layer by the sputtering, there is more oxygen contamination in the aged sample than in the fresh. This suggest that the oxygen can fairly easily diffuse into the structure and is hard to remove. Thus, the aging effect can be seen as a decreasing intensity of Cu $2p$ satellites in the range 940–945 eV and as a narrowing of the Cu $2p_{3/2}$ spectrum which is due to CuO (Cu^{2+}) converting to Cu_2O (Cu^+).

3.7 Discussion: the aging effect

As it was mentioned in the previous sections, the change in the pinning structure can be ruled out, and the time development of XRD, XPS, and magnetisation measurements are best explained by the oxygen release. Particularly, the J_c- and $I(005)/I(00l)$-estimations agree very well, because in both the methods, a steep change is seen in uc-

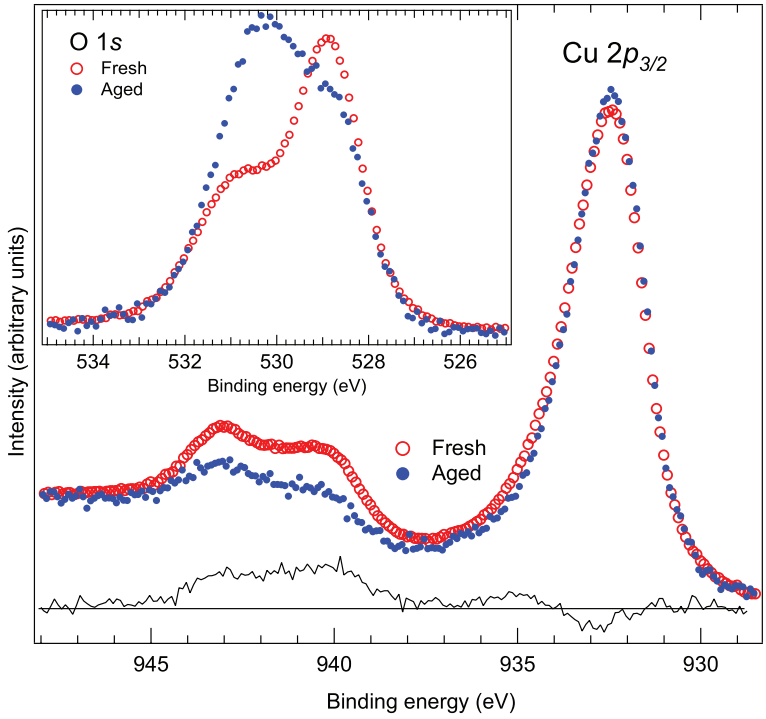

Figure 26. Comparison of Cu $2p_{3/2}$ core-levels and Cu satellite spectra of fresh and aged GdBCO show that the amount of Cu^{2+} has decreased as a function of time. The black line (residue) describes the difference between the Cu $2p$ spectra of fresh and aged samples. From the O $1s$ spectra presented in the inset of figure 26 it can be seen that the oxygen contamination (high BE feature) is much higher for the aged GdBCO despite the similar sputtering treatment of the samples. [**P4**]

and Au-GdBCO for first 1–2 initial months, and no or minor change later, linking these two phenomenon strongly together. Since $I(005)/I(00l)$ measures oxygen content, the lowering of J_c, thus the superconducting properties, originates from the oxygen release.

The reason for the oxygen release is unknown, but because the phenomenon is not seen in YBCO, the probable explanation might be the extra stacking faults not seen in YBCO. The stacking fault might be for example an extra Gd-layer [21], which results in an edge dislocations. The oxygen diffusion is very slow in c-axis direction [153], causing YBCO to be stable, but the diffusion is several magnitudes faster in the ab-planes [153]. Since the oxygen diffusion is as fast through disorders as ab-planes [154], the edge disorders might act as channels for relative fast diffusion towards GdBCO surface. The studies, where YBCO was grown on (110) STO resulting in the ab-planes

to align perpendicular to the substrate surface, have shown similar aging effect [124], and hence confirm this hypothesis. Moreover, it should be noted that the possibility of a protecting layer development onto YBCO but not onto GdBCO can be ruled out, since the Au capping should prevent the growth in both the materials, but the aging effect is only seen for GdBCO.

The reason for oxygen release being faster in Au coated GdBCO in comparison to GdBCO without coating is also unclear. Two explanations are considered. The first one is that Au may form islands on the films rather than grow smoothly layer–by–layer, which is actually confirmed by the AFM measurements done for Au-GdBCO. The forming of such an island might create cracks inside the GdBCO film, causing faster oxygen release. This explanation is weakened by the fact that the sputtering has been done at room temperature, which would not allow Au to attach on GdBCO firmly. On the other hand, this explanation is however supported by the sputtering having an effect on GdBCO, in case if the charge distribution is not disturbed in the surface layer of GdBCO by Au layer. The second possibility is Au acting as a catalyst in GdBCO, as it has been seen for the carbon monoxide and hydrogen oxygenation at low temperatures [155]. Furthermore, as it was showed in the sections 3.2, the GdBCO has a higher surface roughness than YBCO, and such a surface would result in pores of nanosized scale in Au, which would grow the area of the reactive surface and improve the catalyst activity.

4 Conclusions

In this work, it was shown that the YBCO target density can be controlled by the sintering at different temperatures, which have to be between 850°C and 900°C, and the higher is the temperature, the denser is the target. In addition, undoped, 4 wt% BZO-doped and a series of multilayered YBCO, as well as undoped and 4 wt% GdBCO thin films were grown with nanograined targets by pulsed laser deposition on STO (100) single crystals. It was shown that the increasing target density did not influence the pinning structure but decreased the surface roughness of the films. This strengthens the hypothesis that the enhancement of pinning properties in films made from nanograined instead of microngrained target originates really from grainsize.

The growth of GdBCO thin films was optimised for PLD in terms of substrate temperature, T_s, and energy density. The optimised growth temperature was 700°C and energy density 1.8–2.1 J/cm^2 for GdBCO, whereas the optimum conditions were 745°C and 1.8 J/cm^2 for YBCO. Good quality GdBCO films could be ablated in wide temperature range, 625–765°C, and therefore the T_s is not so crucial for GdBCO as for YBCO. All the films fabricated for this work were well textured, and no impurity phases were detected for the fresh films. The twinning structure of GdBCO is very similar to that of YBCO. All the fabricated YBCO films had almost perfect c-orientation, but the volume of a-oriented grains was slightly higher in GdBCO, which was explained by closer c-parameter value to triple value of the lattice parameter of STO, making a-orientation slightly more favourable for GdBCO. It was also shown that the higher J_c's are possible for GdBCO than for YBCO either at low or at high temperatures. It was also shown that GdBCO is more isotropic at high temperatures than YBCO, but at $B \parallel ab$-planes the YBCO had the best pinning potential, U_0, and irreversibility field, B_irr. Therefore, the higher isotropy of GdBCO originates from the lowered intrinsic pinning of Cu–O-planes, which is probably result of the extra stacking faults distorting them.

The BZO was shown to grow cube–on–cube in GdBCO as it is the case in YBCO, and therefore by taking into account the magnetisation measurements, it was confirmed that BZO grows as nanorods in GdBCO. The BZO-doping enhanced the J_c at high fields and low temperatures in GdBCO, similarly as in YBCO. The BZO-doping made also YBCO and GdBCO more isotropic at high temperatures. However, the same BZO-doping level enhanced more the pinning properties (J_c, U_0, B_irr, B^*) of GdBCO at high fields than those of YBCO. This agrees well with twinning structure being more affected by BZO doping in GdBCO than in YBCO. This phenomenon was explained by emerged nanophases with lowered superconducting properties, which may originate

from the cation disorder, extra stress, oxygen deficiency, or all of them together.

The multilayering studies were carried out systematically by varying the layer thicknesses. Therefore the growth process was determined indicating that different thicknesses of multilayers influence the growth mechanism and interlayer structure. The thicker BZO layers usually resulted in worse twinning, in–plane, and out of plane structure, as well as worse superconducting properties, except the temperature dependence of power law exponent, α, which was improved. The only multilayer structure which had pinning properties similar to BZO-doped material was the one where the multilayers were thin and more closely packed. By choosing the right multilayer composition, thick thin films can be fabricated with an actual increase of the critical current.

A worsening of superconducting properties of GdBCO was observed with time, where no such phenomenon was detected for YBCO. The aging was explained by oxygen release occurring via defects not present in YBCO. The Au-coated GdBCO thin film manifested an even worse aging effect, and two possible explanations were suggested: the first is gold acting as a catalyst, and the second is gold producing cracks in the GdBCO matrix.

Thus, if high pinning as possible is needed at high fields, undoped YBCO aligned at $B \parallel ab$-planes should be used, but if high fields and isotropy at low temperatures are needed, BZO-doped GdBCO or closely packed, thin alternating multilayers of YBCO and BZO would probably be the best choices, particularly, if a high current density or thick films are needed.

References

References

[1] H. Onnes, Leiden Comm. **120b, 122b, 124c**, (1911).

[2] W. Meissner ja R. Ochsenfeld, Naturwissenschaft **21**, 787 (1933).

[3] F. London ja H. London, Physica **2**, 341 (1935).

[4] B. Seeber, *Handbook of Applied Superconductivity, Volume 1* (Institute of Physics Publishing Ltd, 1998).

[5] G. Blatter *et al.*, Rev. Mod. Phys. **66**, 1125 (1994).

[6] E. Mezzetti *et al.*, Phys. Rev. B **60**, 7623 (1999).

[7] C. Cai *et al.*, Phys. Rev. B **69**, 104531 (2004).

[8] P. Paturi, M. Irjala, H. Huhtinen ja A. B. Abrahamsen, J. Appl. Phys. **105**, 023904 (2009).

[9] C. J. van der Beek *et al.*, Phys. Rev. B **66**, 24523 (2002).

[10] G. Blatter, V. B. Geshkenbein ja J. A. G. Koopmann, Phys. Rev. Lett. **92**, 067009 (2004).

[11] F. C. Klaassen *et al.*, Phys. Rev. B **64**, 184523 (2001).

[12] P. Paturi, M. Irjala ja H. Huhtinen, J. Appl. Phys. **103**, 123907 (2008).

[13] T. T. M. Palstra *et al.*, Phys. Rev. B **41**, 6621 (1990).

[14] C. W. Hagen ja R. Griessen, Phys. Rev. Lett. **62**, 2857 (1989).

[15] T. T. M. Palstra, B. Batlogg, L. F. Schneemeyer ja J. V. Waszczak, Phys. Rev. Lett. **61**, 1662 (1988).

[16] M. Safonchik *et al.*, Supercond. Sci. Technol. **22**, 065006 (2009).

[17] B. Dam *et al.*, Nature **399**, 439 (1999).

[18] B. M. Lairson, S. K. Streiffer ja J. C. Bravman, Phys. Rev. B **42**, 10067 (1990).

[19] S.-W. Chan, Physica C **55**, 1415 (1994).

[20] D. H. Lowndes *et al.*, Phys. Rev. Lett. **74**, 2355 (1995).

[21] N. Haberkorn, F. Lovey, A. M. Condó ja J. Guimpel, J. Appl. Phys. **97**, 053511 (2005).

[22] S. R. Foltyn *et al.*, Nature materials **6**, 631 (2007).

[23] P. Paturi, H. Huhtinen, K. Laajalehto ja R. Laiho, Supercond. Sci. Technol. **13**, 622 (2000).

[24] H. Huhtinen, P. Paturi, E. Lähderanta ja R. Laiho, Supercond. Sci. Technol. **12**, 81 (1999).

[25] M. Peurla *et al.*, IEEE T. Appl. Supercond. **17**, 3608 (2007).

[26] P. Paturi, M. Peurla, K. Nilsson ja J. Raittila, Supercond. Sci. Technol. **17**, 564 (2004).

[27] F. Sauerzopf, H. Wiesinger, H. Weber ja J. L. G.W. Crabtree and, Physica C **162–164**, 751 (1989).

[28] L. Civale *et al.*, Phys. Rev. Lett. **65**, 1164 (1990).

[29] T. Schuster *et al.*, Phys. Rev. B **47**, 373 (1993).

[30] L. Civale *et al.*, Phys. Rev. Lett. **67**, 648 (1991).

[31] A. Crisan *et al.*, Appl. Phys. Lett. **79**, 4547 (2001).

[32] T. A. Campbell *et al.*, Physica C **423**, 1 (2005).

[33] A. A. Gapud *et al.*, Supercond. Sci. Technol. **18**, 1502 (2005).

[34] C. Cai *et al.*, J. Appl. Phys. **98**, 123906 (2005).

[35] Y. A. Boikov *et al.*, Phys. Rev. B **56**, 11312 (1997).

[36] Q. X. Jia, S. R. Foltyn, P. N. Arendt ja J. F. Smith, Appl. Phys. Lett. **80**, 1601 (2002).

[37] P. N. Barnes, T. J. Haugan, C. V. Varanasi ja T. A. Campbell, Appl. Phys. Lett. **85**, 4088 (2004).

[38] S. Kang *et al.*, Supercond. Sci. Technol. **20**, 11 (2007).

[39] T. Haugan *et al.*, Nature **430**, 867 (2004).

[40] L. Peng *et al.*, J. Phys. D: Appl. Phys. **41**, 155403 (2008).

[41] J. Hänisch *et al.*, Supercond. Sci. Technol. **19**, 534 (2006).

[42] J. Hänisch *et al.*, Appl. Phys. Lett. **86**, 122508 (2005).

[43] T. J. Haugan *et al.*, IEEE T. Appl. Supercond. **17**, 3724 (2007).

[44] C. Cai, B. Holzapfel, J. Hänisch ja L. Schultz, Phys. Rev. B **70**, 064504 (2004).

[45] K. Develos-Bagarinao, H. Yamasaki ja K. Ohki, J. Appl. Phys. **104**, 063907 (2008).

[46] D. B. Jan *et al.*, Appl. Phys. Lett. **82**, 778 (2003).

[47] J. L. MacManus-Driscoll *et al.*, Nat. Mater. **3**, 439 (2004).

[48] A. Goyal *et al.*, Supercond. Sci. Technol. **18**, 1533 (2005).

[49] M. Peurla *et al.*, Supercond. Sci. Technol. **19**, 767 (2006).

[50] K. Traito *et al.*, Phys. Rev. B **73**, 224522 (2006).

[51] H. Huhtinen *et al.*, IEEE T. Appl. Supercond. **17**, 3620 (2007).

[52] Y. Yamada *et al.*, Appl. Phys. Lett. **87**, 132502 (2005).

[53] K. Takahashi *et al.*, Supercond. Sci. Technol. **19**, 924 (2006).

[54] A. Kinoshita *et al.*, Physica C **463-465**, 630 (2007).

[55] T. Kato *et al.*, Physica C **445-448**, 628 (2006).

[56] J. L. MacManus-Driscoll *et al.*, Supercond. Sci. Technol. **23**, 034009 (2010).

[57] T. Horide *et al.*, IEEE T. Appl. Supercond. **17**, 3729 (2007).

[58] T. Horide *et al.*, Supercond. Sci. Technol. **20**, 303 (2007).

[59] M. Peurla *et al.*, Phys. Rev. B **75**, 184524 (2007).

[60] M. K. Wu *et al.*, Phys. Rev. Lett. **58**, 908 (1987).

[61] J. D. Jorgensen *et al.*, Phys. Rev. B **41**, 1863 (1990).

[62] J. Ye ja K. Nakamura, Phys. Rev. B **48**, 7554 (1993).

[63] J. Zaanen, A. T. Paxton, O. Jepsen ja O. K. Andersen, Phys. Rev. Lett. **60**, 2685 (1988).

[64] A. Latge, E. V. Anda ja J. L. Moran-Lopez, Phys. Rev. B **42**, 4288 (1990).

[65] D. de Fontaine, G. Ceder ja M. Asta, Nature **343**, 544 (1990).

[66] C. Andreouli ja A. Tsetsekou, Physica C **291**, 274 (1997).

[67] R. Seppänen *et al.*, *MAOL-taulukot* (Otava, 1991).

[68] J.-I. Shimoyama, S. Horii, K. Otzschi ja K. Kishio, Mat. Res. Soc. Symp. Proc. **689**, 265 (2002).

[69] L. X. Gao *et al.*, J. Appl. Phys. **91**, 1265 (2002).

[70] D. A. Cardwell ja N. H. Babu, Physica C **445-448**, 1 (2006).

[71] H.-R. Yi *et al.*, Appl. Phys. Lett. **56**, 2231 (1990).

[72] R. Krupke *et al.*, Physica C **279**, 153 (1997).

[73] T. Iguchi *et al.*, Supercond. Sci. Technol. **15**, 1415 (2002).

[74] K. Takahashi *et al.*, Supercond. Sci. Technol. **18**, 1118 (2005).

[75] K. Takahashi *et al.*, Physica C **426–431**, 1001 (2005).

[76] A. Ibi *et al.*, Supercond. Sci. Technol. **19**, 1229 (2006).

[77] S. Lee *et al.*, IEEE T. Appl. Supercond. **19**, 3192 (2009).

[78] N. Chikumoto, S. Lee, K. Nakao ja K. Tanabe, Physica C **469**, 1303 (2009).

[79] D. Li ja B. Rosenstein, Phys. Rev. Lett. **90**, 167004 (2003).

[80] J. Raittila, H. Huhtinen, P. Paturi ja Y. P. Stepanov, Physica C **371**, 90 (2002).

[81] U. F. Kocks, C. N. Tome ja H.-R. Wenk, *Texture and anisotropy : preferred orientations in polycrystals and their effect on materials properties* (Cambridge University Press, 2000).

[82] C. P. Bean, Phys. Rev. Lett. **8**, 250 (1962).

[83] C. P. Bean, Reviews of Modern Physics **36**, 31 (1964).

[84] H. P. Wiesinger, F. M. Sauerzopf ja H. W. Weber, Physica C **203**, 121 (1992).

[85] J. Hudner *et al.*, Supercond. Sci. Technol. **7**, 195 (1994).

[86] M. Peurla, H. Huhtinen ja P. Paturi, Supercond. Sci. Technol. **18**, 628 (2005).

[87] H. Huhtinen *et al.*, J. Appl. Phys. **90**, 1521 (2001).

[88] L. C. Pathak *et al.*, J. Mater. Sci **29**, 5455 (1994).

[89] L. C. Pathak, S. K. Mishra, D. Bhattacharya ja K. L. Chopra, Materials Sci. Eng. B **110**, 119 (2004).

[90] J.-S. Kim ja D. R. Gaskell, J. Am. Ceram. Soc. **77**, 753 (1994).

[91] D. B. Chrisey ja G. K. Hubler, *Pulsed Laser Deposition of Thin Films* (John Wiley Sons Inc., 1994).

[92] G. Farnan *et al.*, Supercond. Sci. Technol. **13**, 262 (2000).

[93] F. Fabbri *et al.*, Supercond. Sci. Technol. **13**, 1492 (2000).

[94] A. Marcu, C. Grigoriu, W. Jiang ja K. Yatsui, Thin Solid Films **360**, 166 (2000).

[95] J. M. Huijbregtse, B. Dam, J. H. Rector ja R. Griessen, J. Appl. Phys. **86**, 6528 (1999).

[96] A. Augieri *et al.*, J. Phys. Conf. Ser. **97**, 012209 (2008).

[97] K. Miyachi *et al.*, Physica C **392-396**, 1261 (2003).

[98] P. Liu, Y. W. Zhang ja C. Lu, Appl. Phys. Lett. **80**, 3910 (2002).

[99] A. V. Pan, S. V. Pysarenko ja S. X. Dou, Appl. Phys. Lett. **88**, 232506 (2006).

[100] M. McElfresh *et al.*, J. Appl. Phys. **71**, 5099 (1992).

[101] C. Jooss *et al.*, Physica C **266**, 235 (1996).

[102] H. R. Wenk, A. Chakhmovradian ja S. Foltyn, Materials Science and Engineering A **205**, 9 (1996).

[103] T. Iguchi *et al.*, Physica C **392-396**, 900 (2003).

[104] A. Kaneko *et al.*, Physica C **412-414**, 926 (2004).

[105] R. Kromann *et al.*, J. Appl. Phys. **71**, 3419 (1992).

[106] M. Rand, J. I. Langford, A. Drake ja J. S. Abell, Cryogenics **33**, 291 (1993).

[107] V. Svetchnikov, V. Pan, C. Træholt ja H. Zandbergen, IEEE T. Appl. Supercond. **7**, 1396 (1997).

[108] M. Peurla *et al.*, IEEE T. Appl. Supercond. **15**, 3050 (2005).

[109] B. D. Cullity, *Elements of X-ray diffraction, 2nd ed.* (Addison-Wesley Publishing Company Inc., 1978).

[110] J. Ye ja K. Nakamura, Phys. Rev. B **50**, 7099 (1994).

[111] J. Ye ja K. Nakamura, Physica C **235-240**, 581 (1994).

[112] J. Rodriguez-Carvajal, Abstracts of the Satellite Meeting on Powder Diffraction of the XV Congress of the IUCr 127 (1990).

[113] A. Gauzzi ja D. Pavuna, Appl. Phys. Lett. **66**, 1836 (1995).

[114] X. L. Li, J. Gao, H. Y. Wong ja Z. H. Mai, Thin Solid Films **489**, 200 (2005).

[115] Y. L. Cheung *et al.*, Supercond. Sci. Technol. **20**, 511 (2007).

[116] D. P. Norton *et al.*, Science **274**, 755 (1996).

[117] T. Haugan *et al.*, Physica C **425**, 21 (2005).

[118] F. Peng ja L. Johansson, Journal of Pulp and Paper Science **22**, J252 (1996).

[119] H. Tabata, T. Kawai ja S. Kawai, Phys. Rev. Lett. **70**, 2633 (1993).

[120] A. Verdyan *et al.*, IEEE T. Appl. Supercond. **15**, 3585 (2005).

[121] J. Kawashima, Y. Yamada ja I. Hirabayashi, Physica C **306**, 114 (1998).

[122] S. Yamanaka *et al.*, J. Alloys and Compounds **359**, 109 (2003).

[123] X. J. Chen, C. D. Gong ja Y. B. Yu, Phys. Rev. B **61**, 3691 (2000).

[124] P. Paturi, Private communication.

[125] H. Dai, J. Liu ja C. M. Lieber, Phys. Rev. Lett. **72**, 748 (1994).

[126] Y. R. Sun *et al.*, Phys. Rev. B **51**, 581 (1995).

[127] A. V. Pan ja S. X. Dou, Phys. Rev. B **73**, 052506 (2006).

[128] C. Cai *et al.*, Appl. Phys. Lett. **84**, 377 (2004).

[129] J. M. Huijbregtse *et al.*, Phys. Rev. B **62**, 1338 (2000).

[130] E. Stangl *et al.*, Physica C **256**, 245 (1996).

[131] M. Abdelhadi *et al.*, Appl. Phys. Lett. **88**, 102501 (2006).

[132] M. Hawley, I. D. Raistrick, J. G. Beery ja R. J. Houlto, Science **251**, 1587 (1991).

[133] A. Goyal *et al.*, Supercond. Sci. Technol. **18**, 1533 (2005).

[134] K. Schlesier *et al.*, IEEE T. Appl. Supercond. **19**, 3407 (2009).

[135] L. Hou, J. Deak, P. Metcalf ja M. McElfresh, Phys. Rev. B **50**, 7226 (1994).

[136] K. Kishio *et al.*, Physica C **235-240**, 2775 (1994).

[137] M. Miura *et al.*, IEEE T. Appl. Supercond. **15**, 3078 (2005).

[138] P. Paturi, M. Irjala, A. B. Abrahamsen ja H. Huhtinen, IEEE T. Appl. Supercond. **19**, 3431 (2009).

[139] L. Civale *et al.*, Physica C **412-414**, 976 (2004).

[140] P. Paturi, Supercond. Sci. Technol. **23**, 025030 (2010).

[141] A. Gurevich ja E. A. Pashitskii, Phys. Rev. B **56**, 6213 (1997).

[142] J.-P. Locquet *et al.*, Nature (London) **394**, 453 (1998).

[143] T. Hwa, P. L. Doussal, D. R. Nelson ja V. M. Vinokur, Phys. Rev. Lett. **71**, 3545 (1993).

[144] L. Civale *et al.*, Phys. Rev. B **50**, 4102 (1994).

[145] B. Maiorov *et al.*, Nat. Mater. **8**, 398 (2009).

[146] J. H. Weaver *et al.*, Phys. Rev. B **38**, 4668 (1988).

[147] H. Behner, K. Rührnschopf, W. Rauch ja G. Wedler, Applied Surface Science **68**, 179 (1993).

[148] Y. A. Teterin, M. I. Sosulnikov ja Y. A. Petrov, Journal of Electron Spectroscopy and Related Phenomena **68**, 469 (1994).

[149] J. Beyer *et al.*, Physica C **246**, 156 (1995).

[150] J. Ghijsen *et al.*, Phys. Rev. B **38**, 11322 (1988).

[151] G. G. Jernigan ja G. A. Somorjai, Journal of Catalysis **147**, 567 (1994).

[152] A. Hartmann, G. J. Russell ja K. N. R. Taylor, Physica C **205**, 78 (1993).

[153] S. J. Rothman, J. L. Routbort, U. Welp ja J. E. Baker, Phys. Rev. B **44**, 2326 (1991).

[154] A. Kursumovic *et al.*, Physica C **331**, 185 (2000).

[155] M. Haruta, N. Yamada, T. Kobayashi ja S. Iijima, Journal of Catalysis **115**, 301 (1989).